UNIVERSIDAD DE INVESTIGACIÓN DE TECNOLOGÍA EXPERIMENTAL YACHAY

Escuela de Ciencias Físicas y Nanotecnología

TÍTULO: Synthesis Optimization for Reduced Graphene Oxide-based Electrodes from Surface Modified Silica Fibers

Trabajo de Integración curricular presentado como requisito para la obtención del título de ingeniería en Nanotecnología

Autor:

De la Torre Oyola María Jose

Tutor:

PhD Chacón-Torres Julio César

Urcuquí, Julio 2021

SECRETARÍA GENERAL
(Vicerrectorado Académico/Cancillería)
ESCUELA DE CIENCIAS FÍSICAS Y NANOTECNOLOGÍA
CARRERA DE NANOTECNOLOGÍA
ACTA DE DEFENSA No. UITEY-PHY-2021-00018-AD

A los 29 días del mes de julio de 2021, a las 12:00 horas, de manera virtual mediante videoconferencia, y ante el Tribunal Calificador, integrado por los docentes:

Presidente Tribunal de Defensa	Dr. VACACELA GOMEZ, CRISTIAN ISAAC , Ph.D.
Miembro No Tutor	Dr. CHIMBORAZO GUERRON, JOHNNY FABRICIO , Ph.D.
Tutor	Dr. CHACON TORRES, JULIO CESAR , Ph.D.

El(la) señor(ita) estudiante **DE LA TORRE OYOLA, MARIA JOSE**, con cédula de identidad No. **0951517176**, de la **ESCUELA DE CIENCIAS FÍSICAS Y NANOTECNOLOGÍA**, de la Carrera de **NANOTECNOLOGÍA**, aprobada por el Consejo de Educación Superior (CES), mediante Resolución **RPC-SO-13-No.156-2015**, realiza a través de videoconferencia, la sustentación de su trabajo de titulación denominado: **SYNTHESIS OPTIMIZATION FOR REDUCED GRAPHENE OXIDE-BASED ELECTRODES FROM SURFACE MODIFIED SILICA FIBERS**, previa a la obtención del título de **INGENIERO/A EN NANOTECNOLOGÍA**.

El citado trabajo de titulación, fue debidamente aprobado por el(los) docente(s):

Tutor	Dr. CHACON TORRES, JULIO CESAR , Ph.D.

Y recibió las observaciones de los otros miembros del Tribunal Calificador, las mismas que han sido incorporadas por el(la) estudiante.

Previamente cumplidos los requisitos legales y reglamentarios, el trabajo de titulación fue sustentado por el(la) estudiante y examinado por los miembros del Tribunal Calificador. Escuchada la sustentación del trabajo de titulación a través de videoconferencia, que integró la exposición de el(la) estudiante sobre el contenido de la misma y las preguntas formuladas por los miembros del Tribunal, se califica la sustentación del trabajo de titulación con las siguientes calificaciones:

Tipo	Docente	Calificación
Miembro Tribunal De Defensa	Dr. CHIMBORAZO GUERRON, JOHNNY FABRICIO , Ph.D.	9,2
Presidente Tribunal De Defensa	Dr. VACACELA GOMEZ, CRISTIAN ISAAC , Ph.D.	9,5
Tutor	Dr. CHACON TORRES, JULIO CESAR , Ph.D.	8,5

Lo que da un promedio de: **9.1 (Nueve punto Uno)**, sobre 10 (diez), equivalente a: **APROBADO**

Para constancia de lo actuado, firman los miembros del Tribunal Calificador, el/la estudiante y el/la secretario ad-hoc.

Certifico que *en cumplimiento del Decreto Ejecutivo 1017 de 16 de marzo de 2020, la defensa de trabajo de titulación (o examen de grado modalidad teórico práctica) se realizó vía virtual, por lo que las firmas de los miembros del Tribunal de Defensa de Grado, constan en forma digital.*

DE LA TORRE OYOLA, MARIA JOSE
Estudiante

Dr. VACACELA GOMEZ, CRISTIAN ISAAC , Ph.D.
Presidente Tribunal de Defensa

Dr. CHACON TORRES, JULIO CESAR , Ph.D.
Tutor

Dr. CHIMBORAZO GUERRON, JOHNNY FABRICIO , Ph.D.
Miembro No Tutor

CIFUENTES TAFUR, EVELYN CAROLINA
Secretario Ad-hoc

AUTORÍA

Yo, **María Jose De la Torre Oyola**, con cédula de identidad 0951517176, declaro que las ideas, juicios, valoraciones, interpretaciones, consultas bibliográficas, definiciones y conceptualizaciones expuestas en el presente trabajo; así como: los procedimientos y herramientas utilizadas en la investigación, son de absoluta responsabilidad de el/la autor (a) del trabajo de investigación curricular. Así mismo, me acojo a los reglamentos internos de la Universidad de Investigación de Tecnología Experimental Yachay.

Urcuquí, Julio 2021.

María Jose De la Torre Oyola

CI: 0951517176

AUTORIZACIÓN DE PUBLICACIÓN

Yo, **María Jose De la Torre Oyola**, con cédula de identidad 0951517176, cedo Universidad de Investigación de Tecnología Experimental Yachay, los derechos de publicación de la presente obra, sin que deba haber un reconocimiento económico por este concepto. Declaro además que el texto del presente trabajo de titulación no podrá ser cedido a ninguna empresa editorial para su publicación u otros fines, sin contar previamente con la autorización escrita de la Universidad.

Asimismo, autorizo a la Universidad que realice la digitalización y publicación de este trabajo de integración curricular en el repositorio virtual de conformidad a lo dispuesto en el Art. 144 de la Ley Orgánica de Educación Superior.

Urcuquí, Julio 2021.

_____
María Jose De la Torre Oyola
CI: 0951517176

Abstract

In this thesis work, it is proposed an innovative methodology for the preparation of reduced graphene oxide optimized for surface modified silica nanoelectrodes (rGO/OF). Aqueous chemical reduction of graphene oxide (GO) was carried by using sodium borohydride as a function of time from 3 h to 42 h, in order to recover the electrical properties of graphene. Samples of rGO/OF were characterized in Raman spectroscopy. Raman spectra results showed that the longer the reduction time it is possible to obtain a graphitic material with fewer oxygen-containing functional groups. The optical fiber (OF) surface was modified by treatment at 700 °C in an oxidizing environment and 1:3 piranha solution for polymeric coatings removal; and subsequently (3-aminopropyl)triethoxysilane (APTES) was used for adhesion of concentric rGO to the OF. The characterization results confirm the feasibility of rGO as a conductive material for miniaturized sensing devices.

Keywords: graphene synthesis, rGO, Raman spectroscopy, chemical reduction.

Resumen

En este trabajo de tesis, se propone una metodología innovadora para la preparación de óxido de grafeno reducido optimizado para nanoelectrodos de sílice de superficie modificada (rGO/OF). La reducción química acuosa del óxido de grafeno (GO) se llevó a cabo usando borohidruro de sodio (NaBH$_4$) en función del tiempo de 3 h a 42 h, con el fin de recuperar las propiedades eléctricas del grafeno. Las muestras de rGO/OF se caracterizaron en espectroscopía Raman. Los resultados de los espectros Raman mostraron que cuanto mayor es el tiempo de reducción es posible obtener un material grafítico con menos grupos funcionales que contienen oxígeno. La superficie de la fibra óptica (OF) se modificó mediante tratamiento a 700 °C en un ambiente oxidante y una solución de piraña 1:3 para la eliminación de recubrimientos poliméricos; y posteriormente se utilizó (3-aminopropil) trietoxisilano (APTES) para la adhesión de rGO concéntrico al OF. Los resultados de la caracterización confirmar la viabilidad de rGO como material conductor para dispositivos de detección miniaturizados.

Palabras clave: síntesis de grafeno, rGO, espectroscopia Raman, reducción química.

Acknowledgements

I would like to thank her that has always shaken me for making the best of my todays be the worst of my tomorrows. Special thanks of gratitude to my family for giving me all they have. Sincerely thanks to the witnesses of this journey my advisor Julio C. for challenged me and spent time supporting me on this project. This was not easy, especially with an ongoing pandemic. Also, thanks to Gottfried S. and Gema G., who beyond academics I consider them life advisors, for this scientific life that I just got into.

When I look back to the beginning when I first arrived at Yachay Tech University, I could not explain to myself that technological development is so within reach of Ecuador that you could not just be a spectator but be part of that development. Thanks to every one of my professors at Yachay Tech, for all your advice, your life stories, cheering and encouragement.

Friends are often there to help you work out problems and to give you another perspective on things you are passing through. I want to thank my lifelong friends: Kris, Anggie, Sonia, Joel, Alexis, Adrian who always respond even when months go by. I cannot explain how lucky I am to meet such wonderful people during this five-year journey, thanks to my latest friends: Dani, Sebas, Pablo, Francis, Vicky, Gene, Kimi, Cris, Ariel, Produccion Team, Innomaps Team, SDSN Hub, and so many that this page would fill, with whom I have shared the most incredible adventures along with my college life and I wish the best for them. Thanks to Nico, for always encourage me to keep trying but try harder.

Thank you all for enjoying life with me.

Dedication

To my future self
"Maybe it is dumb to look out for signs in the universe, maybe there aren't any signs. Maybe a locket is just a locket and a chair is just a chair. Maybe we don't need the universe to tell us what we really want. Maybe we already know that. Deep down." Do not settle, "it is funny how sometimes you just find things."

Contents

List of Figures

List of Tables

Chapter 1

Introduction

The desire to increase the sensitivity and to reduce the response times of electrochemical sensing devices has prompted the development of miniaturized electrochemical sensors (MEC).[1] In comparison with macroscale sensing systems that requires expensive and bulky equipment and time-consuming processes, micro and nanoscaled electrochemistry presents advantages like portability, target detection, and short analysis time.[2] High attention is being paid for applications like health care,[3] energy generation and storage devices,[4] touchscreens and flexible electronics,[5] inter/intracellular measurements,[6] and environmental monitoring.[7] However, three fundamental challenges still have to be addressed for MECs: First, an accurate and reproducible fabrication that is essential for sensing devices. Second, massive fabrication expenses due to the introduction of new fabrication processes. Third, synthesis of a material with outstanding electron transfer properties, which is fundamental for electrochemical cells. For this purpose, graphene results in a promising candidate for the fabrication of MECs. Graphene is a two-dimensional (2D) single-layer nanomaterial that can reach high electrochemical activity because its carbon atoms are exposed on the surface making graphene able to detect any change in the surroundings.[8] The conductance behavior at its Dirac points gets boosted due to its free-π electrons and electrons holes have zero-effective mass,[9] which linear dispersion relation between the conduction band and valence band form two inverted cones with the tips touching at the Fermi energy, corresponding to a zero-gap semiconductor.[9] To produce high conductive graphene, graphite, which is the stacked arrangement of carbon atoms layers, has to be reduced to mono-layer and stripped of various oxygen-containing functional groups (-CO, -OH, -COOH), which produce

a band-gap greater than 1.5 eV.[10] When the material gets modified to reduced graphene oxide (rGO), it exhibits a large surface area, wide electrochemical potential window, and high tuneable behavior by chemical doping.[9] In this way, graphene-based electrodes are capable of providing more sensitive interfaces due to increased surface area and faster electron transfer.[9,11] Clearly, the main challenge lies in obtaining high-quality graphene while being able to produce it on a large scale. In this project, an optimized chemical reduction synthesis was carried out by using $NaBH_4$, which changes the game for offering a simpler and more affordable technique,[12] that has been shown to produce the least defective sites and to reduce oxygen functional groups to a large extent, making this method appropriate for recovering the electrical conductivity properties of rGO (near-pristine), at large-scale fabrication. Despite the challenges, many researchers have developed novel graphene-based MEC sensors, where the material for working electrodes is made of silica. Glassy carbon electrodes exhibited a lower limit of detection and could efficiently mediate the charge transfer.[13] A reference for this work, a novel graphene micro-ring electrode was fabricated by Dickinson et al[14] and they suggest this arrangement of graphene on optical fiber (OF) makes it possible to exploit greater electrochemical activity of graphene's edge sites. The graphene ring microelectrode (GRiME) exhibits a wider electrochemical window than glassy carbon in aqueous electrolytes while also claiming the absence of oxygen functionalities. The possibility to generate electrodes of sub-nm dimensions cost-effective MEC sensors[14] could be helpful for heavy metals environmental monitoring.

1.1   Problem Statement

Graphene material obtained from current chemical synthesis has shown high electron transfer and response time. The main challenge in this project is to synthesize rGO by an affordable chemical method and identify the degree of functionalization (specifically oxygen-containing functional groups) through Raman characterization of the resulting samples.

1.2 Objectives

1.2.1 General Objective

In nanoelectronics it is necessary to understand and ensure the proper fabrication of the electrodes in nano/micro scales attain raised efficiency of the material. In this way, this study aspires to explore a novel design of high-performance miniaturized electrodes based on rGO for surface-modified silica fiber.

1.2.2 Specific Objectives

1. Modify the surface of OF electrodes with 3-aminopropyltiethoxysilane (APTES).

2. Propose an optimized chemical oxygen reduction method that recovers the electrical properties of graphene.

3. Characterize the rGO material by Raman spectroscopy.

4. Deposite rGO along OF electrode by using the reference methodology.

5. Characterize the surface of electrodes and the oxygen content of rGO, by using SEM and Raman spectroscopy, correspondingly.

1.3 Organization of Thesis

This document has been divided into five chapters: Introduction, Theoretical Background, Methodology, Results and Discussion, Conclusions, and Outlook. Chapter 1 swiftly presents the motivation and scope of this project, the problem statement, and the general and specific objectives expected to be accomplished in this work. Chapter 2 exposes a detailed review of graphene. its derivatives and graphene's properties of interest like the chemical structure and the electrical conductivity, and the reducing processes to enhance these properties. Chapter 3 shows the optimized methodology for obtaining rGO, while Chapter 4 provides the results from Raman spectroscopy characterization. Finally, Chapter 5 presents the conclusions and achieved

objectives, and also proposes future work based on the results obtained here.

Chapter 2

Theoretical Background

This chapter is a brief introduction of the field of nanotechnology, as well as the well-known material graphene. Different synthesis methods and their resulting performance in terms of chemical characteristics, defects, quality, costs, scale production, among others, will be outlined. Reduction of graphene by chemical method, which is the approach of interest in this project, will be presented in detail. Optical fiber material and its characteristic as a working electrode will be addressed. Finally, the main characterization techniques, Raman spectroscopy and Scanning Electron Microscopy used in this project will be described.

2.1 Nanotechnology

The etymology of nanotechnology proceeds from the Greek word *nanos*, used to name *dwarf*, and measures a billionth part of a meter (10^{-9} m), the size of the atoms[15]. "There is plenty of room at the bottom", were the words Richard P. Feynman (May 11, 1918 - February 15, 1988) used to describe the astonishing prospects to work at the subatomic scale, in his talk at the annual meeting of the American Physical Society at California Institute of Technology[16]. Feynman was challenged with the miniaturization of the information by writing the entire 24 volumes of the *Encyclopaedia Britannica* on the head of a pin[16]. Those were the first notions of nanotechnology, although this term was not conceived in 1959. In the following years, the rearrangement of atomic information was essential for the structure of the Internet. A nanometric particle or material can be defined as nanomaterial when one or more of its geometrical dimensions has a size between 1

nm to 100 nm. By working with nanomaterials, the idea of an atom-by-atom precision assembly is feasible and also a complete redesign of materials and devices with improved characteristics and properties.[15] However, when reducing the dimensions it has to be taken into account the gross performance obtained from the resultant nanomaterial, in terms of an input-output relation. Aspects like property enhancement, large scale-production, accurate design, total energy required, and functional response are of great interest. In this way, nanotechnology is an emerging and disruptive technology that allows for the possibility to manipulate matter at a nanometric scale to produce materials with novel design, structure, and properties.[17] The major properties of interest in this project, for the design of a sensing apparatus are the enhanced electronic properties found in the novel nanomaterial, graphene. Graphene, and all carbon-based nanomaterials in general, has demonstrated rising optoelectronic, electronic, structural, thermal, and mechanical properties due to its singular confinement of electrons and symmetry.[18]

2.2 Graphene

Graphene is a two-dimensional (2D) nanomaterial with a honeycomb shape. This allotropy of carbon was first synthesized at the University of Manchester in 2004 by Andre Geim and Konstantin Novoselov, who won the Nobel Prize of Physics in 2010.[8] A single layer of graphene is the elemental structure for all the carbon based nanomaterials; by comparing a sheet of paper with a sheet of graphene,[9,19] it can be wrapped up to form a fullerene (0D), rolled up to form a nanotube (1D), or stacked up to form graphite (3D); above, middle, and below, respectively, as shown in Figure 2.1. These mentioned allotropes cannot simply be manipulated as a sheet to obtain these shapes, but each one needs a different chemical or physical synthesis methods, such as chemical vapor deposition or arc discharge technique; for this reason, it is important to develop methods that allow achieving the desired structures and properties.[19] A single layer of graphite has fundamental properties that made it the ideal material for structural, optical, and electrical applications.[18] A perfect graphene sheet can, theoretically, show a surface area of 2630 m^2 g^{-1} and ultra intrinsic charge carrier mobility of 200,000 cm^2 V^{-1} s^{-1}.[20] An indention test of suspended graphene yielded 130 GPa,[21] which proportion strength-density is about 100 times stronger than the strongest steel, while its density is significantly lower than any steel, with a surface mass of 0.763 mg per square meter. The record for the strongest known material with a

breaking strength of 42 N/m. While it is strong it remains very flexible with Young's modulus of 1 TPa.[21] These promising features make of graphene useful for the implementation and development of electronic devices such as batteries, photovoltaics, capacitors, sensors, energy storage, transducers, and material enhancement.[20,21,23] To achieve these theoretical properties and, as consequence, lead to the applications mentioned, graphene needs to be isolated from the multiple layers of graphite so a high recovery of electrical conductivity properties of graphene oxide can be achieved. Graphene-based electrochemical devices contribute with higher sensitivity to electrodes,[23] because of high electron transfer and response time. In this work, the technique that most enhances the electrical properties will be sought.
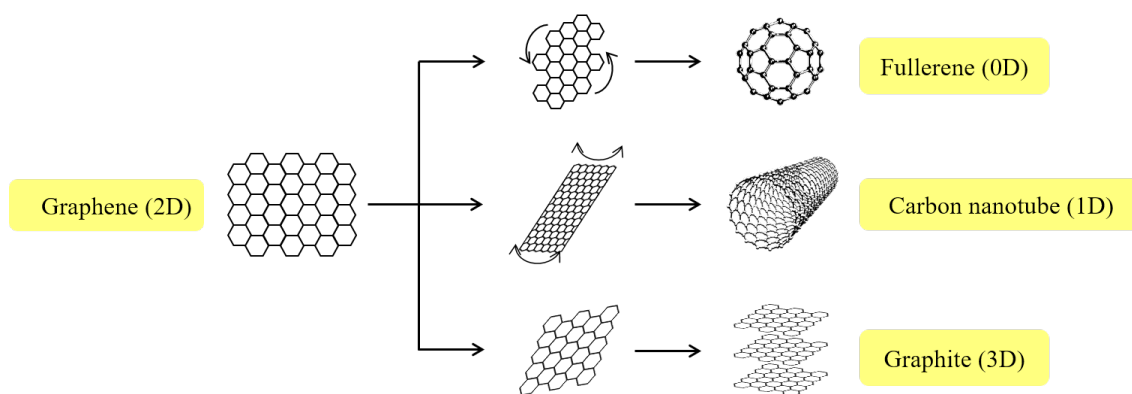
Figure 2.1: Different shapes of carbon allotropes made up from a sheet of graphene (2D) by different synthesis methods. From top to bottom: fullerene (0D), carbon nanotube (1D), and graphite (3D). Adapted from Bhuyan et al.[19]

2.2.1   Structural properties

Graphene is a single planar sheet of graphite, packed in a honeycomb-like crystal lattice made up of carbon with sp^2 hybridization.[9,24] Graphene has three sp^2 type hybridization bonds; one s and two p orbitals, p_x and p_y, at each carbon atom mix to form 3 in-plane equivalent orbitals with σ bonds; and finally, a π orbital perpendicular to the plane.[9] The main properties of graphene are influenced by its hybridization, which is the mixing of valence electronic states. The in-plane σ_{C-C} bond is much stronger than the energy difference between $2s$ and $2p$ orbitals, for this reason these

orbitals can get mix in a configuration of sp^n (with n = 1, 2, 3). When a carbon atom in graphene gets bonded with its other three carbon neighbors, each one arranged with 120 degrees of separation, it results in hybrid orbitals with sp^2 configuration, this is shown in Figure 2.2. In diamond, on the other hand, each carbon atom has four carbon neighbors, separated by 109.5 degrees, which results in a sp^3 hybridization.[26] In sp^2 configuration, $2s$ and $2p$ orbitals get mixed to form three in-plane covalent bonds, which are the strongest bonds known in nature so far, even stronger than diamond sp^3 bonds, and forms linear chains of carbon atoms interconnected in a hexagonal ring.[26]
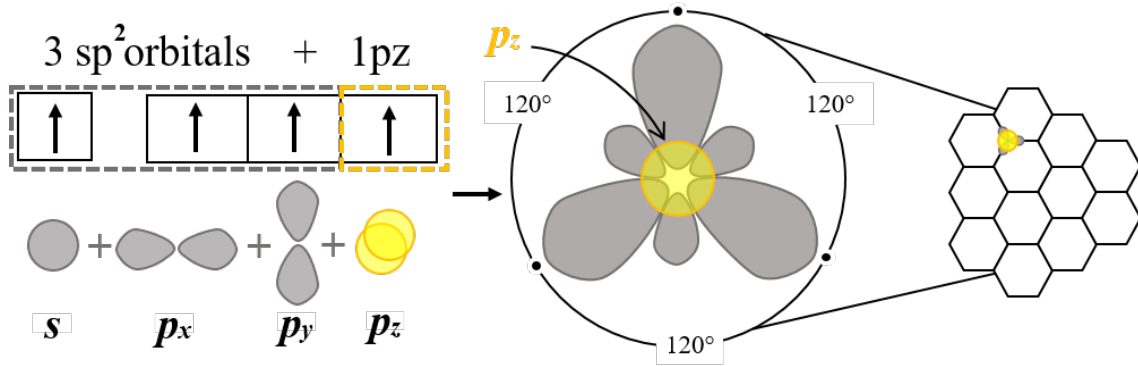
Figure 2.2: Electron promotion from *s* state to *p* state to form three *sp^2* hybrid orbitals (and one p$_z$) in graphene electronic configuration. Graphene differs from other carbon materials due to the high strength in σ_{C-C} bonds.

As shown in (a) in Figure 2.3, electron promotion from the ground state allows the formation of three σ (bonding) and three σ^* (anti-bonding) orbitals, in gray, and π and π^* orbitals, in yellow. Two carbon atoms A (black) and B (white) form the primitive cell in the crystal lattice of graphene. Each σ_{C-C} bond, red arrow, between carbon atoms have a distance of 0.142 nm (1.42 Å); while the red dashed lines in (a) highlight the σ bonds of atoms forming the hexagonal lattice. The unit cell has a rhombus shape formed by the unitary vectors a_1 and a_2.[9] The magnitude of these vectors forming the real space can be represented in Cartesian coordinates as follows:

$$a_1 = \frac{a}{2} \left(\sqrt{3}\,\hat{x},\ \hat{y} \right) \qquad \text{and} \qquad a_2 = \frac{a}{2} \left(\sqrt{3}\,\hat{x},\ -\hat{y} \right), \tag{2.1}$$

In this way, $|a_1| = |a_2| = 2.46$ Å form the yellowish rhombus of the unit cell of graphene.

Besides, the diffraction of the lattice is not a direct representation of the real lattice, but the reciprocal lattice. The reciprocal lattice is constructed by the Fourier transform of the real lattice of a physical space, in which an array of vertices can be represented by primitive vectors in a Bravais lattice. In a graphene monolayer, the vectors in reciprocal space are represented as b_1 and b_2, in (b) in Figure 2.3. It is presented the first Brillouin zone (in gray), showing the first region (primitive cell) of the reciprocal lattice and the symmetry points Γ, K, K' and M, which describes the propagation of the waves in a periodic medium.[9] Vectors b_1 and b_2 are rotated 30° from the real space vectors, respectively, and are represented in Cartesian coordinates in the following way:

$$b_1 = \frac{2\pi}{a} \left(\frac{1}{\sqrt{3}} \hat{x}, \, \hat{y} \right) \qquad \text{and} \qquad b_2 = \frac{2\pi}{a} \left(\frac{1}{\sqrt{3}} \hat{x}, \, -\hat{y} \right), \qquad (2.2)$$

The Brillouin zone in graphene is defined by the relation of the reciprocal lattice and **K** wave vectors that belong to it, satisfying the relationship:

$$e^{(iK \cdot R)} = 1 \qquad (2.3)$$

for all **R** Bravais lattice points.

The symmetry of a monolayer graphene is an isotropic planar with space group P6/mm;[27] however, the crystal structure of graphene can be changed by functionalization, corrugation, defect formation; at the same time, several properties like electrical, optical, topological, and chemical would change. Synthesis methods are the main aspect that sets different lattice vectors and interatomic distances.

2.2.2 Electronic properties

Carbon-based nanomaterials have been found ideal for electronic devices, special graphene with its two-dimensional shape behaves like a semiconductor while having no band-gap. As mentioned before, in the chemical structure section, graphene has a sp^2 hybridization orbitals that forms three σ bonds between carbon atoms[21,51]. The remaining p orbitals can get bind with other atoms
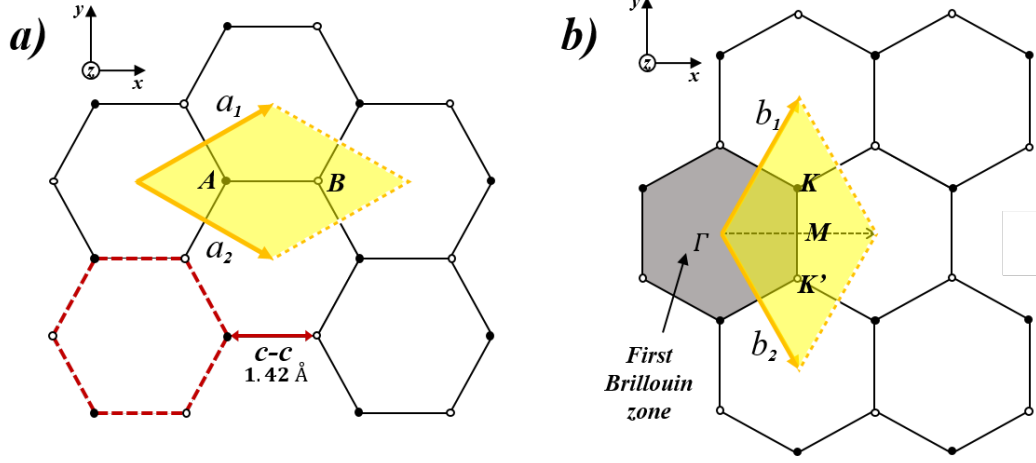
Figure 2.3: Layer of graphene with its (a) real space unit vectors defined by a_1 and a_2 and the reciprocal lattice (b) defined by b_1 and b_2. Adapted from[40]

and form a very weak interplanar van der Waals interaction, π bond[21]. Each p orbital is half-filled with free π electrons that can move around in the valence band. Points K and K' are located in the corners of the hexagonal First Brillouin zone where, the so-called Dirac points, converge with vectorial positions:[9].

$$K = (\frac{2\pi}{3a}, \frac{2\pi}{3\sqrt{3}a}), \qquad\qquad K' = (\frac{2\pi}{3a}, -\frac{2\pi}{3\sqrt{3}a}) \qquad\qquad (2.4)$$

Tight binding mathematical interpretation is given by the Hamiltonian of a single carbon atom, in a 2x2 matrix where the eigenfunctions are the atomic orbitals of the carbon, as follows[51]

$$\hat{H} = \sum_k \Psi^* h(k) \Psi \qquad\qquad (2.5)$$

where

$$\Psi \equiv \begin{pmatrix} \hat{a}_k \\ \hat{b}_k \end{pmatrix}, \qquad\qquad \Psi^* \equiv \begin{pmatrix} \hat{a}_k^* & \hat{b}_k^* \end{pmatrix}, \qquad\qquad (2.6)$$

and

$$\mathbf{h(k)} \equiv -t \begin{pmatrix} 0 & \Delta_k \\ \Delta_k^* & 0 \end{pmatrix} \qquad\qquad (2.7)$$

Where $\hat{a}_k$, $\hat{a}_k^*$, $\hat{b}_k$, and $\hat{b}_k^*$ are fermionic operators, t is t with a value of 2.8eV. Then, resulting Hamiltonian is

$$\Delta_{\mathbf{k}} \equiv \sum_{\delta} e^{i\mathbf{k}\cdot\delta} \tag{2.8}$$

By solving Δ_k, the eigenvalues for the matrix are given by

$$\varepsilon_{(k_x,k_y)}^{\pm} = |\Delta_k| = \pm t_0 \sqrt{\Delta_k \Delta_k^*}, \qquad \varepsilon_{(k_x,k_y)}^{\pm} = |\Delta_k| = \pm t_0 \sqrt{1 + 4 \, \cos\frac{\sqrt{3}k_x a}{2} \cos\frac{k_y a}{2} + \cos^2\frac{k_y a}{2}} \tag{2.9}$$

For points k-space (Brillouin zone) where the eigenvalues are $\varepsilon_{\pm}(\mathbf{k}) = 0$. This demonstrates graphene is a zero-gap semiconductor. However, in the next section the electronic states. [21]

Energy Band Structure

The property of electrical conductivity of a material is defined by the ability of electrons to flow in different electronic states. Energy bands are associated with the most closely spaced orbitals and can be considered as a continuum or discrete energy level. [9] From this, valence and conduction bands can be distinguished. Valence electrons, which are the outermost shell electrons in the atom, are responsible for jumping from valence to conduction band, when excited, and become a charge carrier as long as the conduction band provides a vacant. [9] If this occurs, a hole will be left in the valence band. Certain ranges or energy levels that may or may not be allowed to occupy. Forbidden levels are called band-gaps, which separate the valence band from the conductivity band. [51] At the bandgaps electrons cannot circulate freely, but while having enough amount of energy to overcome it. In other words, it is called the bandgap the energy required for an electron to jump from one band to another. In graphene, the conduction band and valence band meet at the Dirac points; in conclusion, graphene is a zero-gap semiconductor. [51]

Graphene acts like a semiconductor while having a zero band-gap, which is represented in Figure 2.4 side a), where the Dirac cone tips are touching at the Fermi level, which is the highest energetic level occupied by the electrons. Side b), instead, displays the electronic bands of a graphitic or graphene oxide material, in which the density of the state is high but the oxygen functionalities, like carboxylic, hydroxyl, and carbonyl groups at the basal and edge planes, offset the Fermi energy higher than 0. [51] In this way the electrical conductivity properties are quenched.

On the C side, the bandgap have been reduced as graphene have reduced the amount of oxygen groups in its structure, then the conductivity properties can arise.
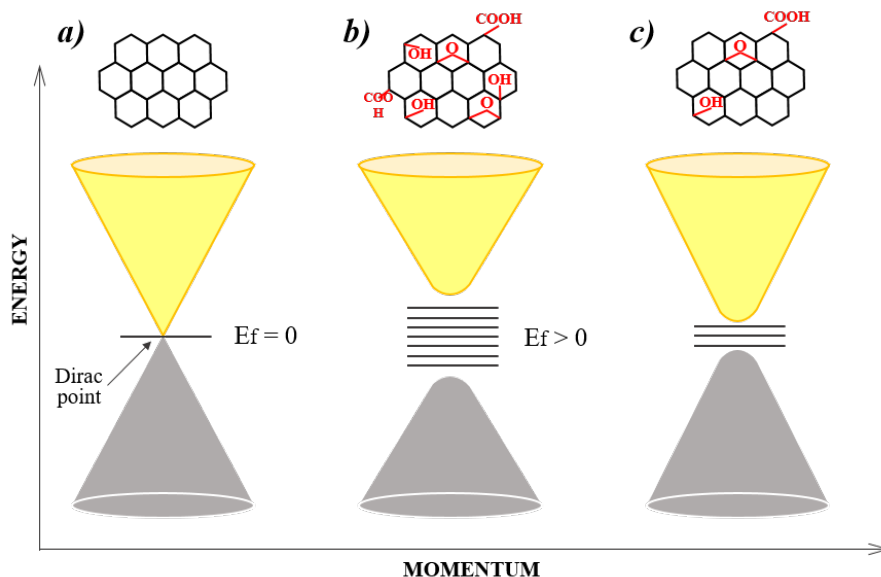
Figure 2.4: Representation of the momentum and energy of the Dirac cone of a) graphene, b) graphene oxide with oxygen functionality groups such as carboxylic, hydroxyl, and carbonyl groups at the surface and edges, and c) reduced graphene oxide with a reduced amount of groups.

2.2.3   The effects of the defects

It is a universal truth that all systems, graphene included, have a level of disorder, in compliance with the second law of thermodynamics. Even when we talk about thermal equilibrium. As mentioned above, changes in the electronic structure of graphene affect its electronic properties in the same way. Different types of disorder can occur in the lattice by topological, impurity, and self-doping states.

Near Dirac point and other short-range interactions. While mean free path of electrons in general conductor materials reach nanometer ranges, electrons in graphene can reach 1 μm.[51] Where mean free path can be defined as the average length a particle can travel before changing its

momentum. Ballistic transport can be afforded since electrons move like particles with zero mass and hardly scatter when transporting.[51] Without scattering, electrons follow Newton's second law of motion at non-relativistic speeds. This is very important for conduction at nanodevices since charge-carriers flow in a medium without resistivity. However, near Dirac points, graphene shows very low electron transfer, about $4e^2/h$, near its Dirac points.[9]

Self-doping and Defects States. On the other hand, graphene material and derivatives (GO, rGO) will have defects related to the high reactivity of the sp^2 hybridized carbon atoms, which will introduce bond rotation that will allow the appearance of pentagons and heptagons in the structure.[9] Graphene distorted states can be categorized into two: Extrinsic (vacancies,) and intrinsic (ripples and topological defects).[9] These of doping effects are produced when p-type donors or acceptors are introduced, then the resulting material becomes more willing to receive electrons thanks to the greater presence of free holes. Boron doping, for example, which has one less electron, encourages negative charges to fill these holes.[22] On the other hand, when introducing n-type or donor elements, there is an excess of negative charge that produces a greater conduction of electrons, this occurs when doping graphene with nitrogen, for example.

Topological defects. The topological disorder can be seen due to the presence of impurities and the addition of functional groups. For this thesis, topological disorders caused by the insertion of oxygen-containing functional groups will be considered. Yan et al.[50] detailed in their work about oxidation functional groups of graphene, epoxy, and hydroxy. In an epoxy group, the bond distance between C — O is 1.44 Å, while in plane C — C atoms are 1.42 Å. O atom, at the top and connected with two C atoms from the main structure, moves upward the lattice 0.37 Å which enlarges the C — C bond length to 1.48 Å, this is shown in a) in Figure 2.5. While side b) shows the hydroxyl group forms a new C — O — H angle of 107.9°, larger than the angle in H_2O (104.4°); likewise, the bond length is 0.98 Å for H — O, while 0.96 Å for H_2O.[50]

2.2.4 Synthesis methods

In general, nanomaterials can be produced from a top-down (TD) approach or bottom-up (BU) approach. In TD approaches the size of the material is reduced to nanoparticles or nanostructures. The most common TD methods are photolithography, nanoimprint lithography (NIL), electron
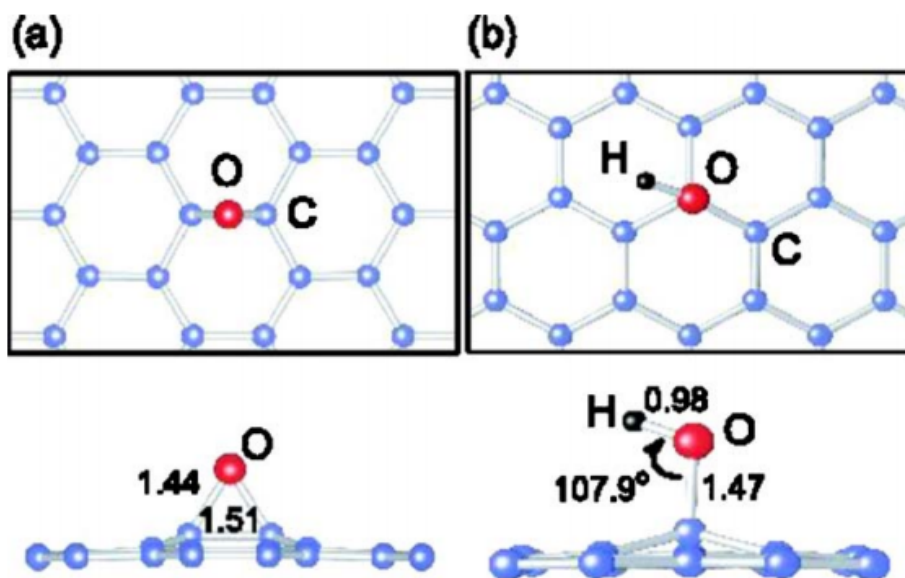
Figure 2.5: Epoxy (a) and hydroxyl (b) functional groups that result in topological defects for lattice structure of graphene. Adapted from Yan et al.[50]

beam lithography (EBL), reactive ion etching (RIE), and deep reactive ion etching (DRIE). In BU approaches, atom-by-atom and molecule-by-molecule are arranged and clustered together to reach a nanostructure. The most common BU methods are chemical vapor deposition (CVD), physical vapor deposition (PVD), pyrolysis, and emulsification. Regarding its main disadvantages, TD methods entail more complicated processes since they demand a lot of energy for cutting down the bulk material to the nanoscale, while BU methods are time-consuming and face challenges to scalability.[47] Specifically, graphene can be synthesized by several techniques from both approaches. For the top-down approach, the graphitic bulk material gets destroyed through mechanical exfoliation including cleaving, arc-discharge method, atomic force microscope (AFM) cantilever exfoliation, sonication or liquid-phase exfoliation (LPE), electrochemical exfoliation, and reduced graphene oxide synthesis. For bottom-up techniques, graphene can be built up from carbon structures; including pyrolysis, unzipping carbon nanotubes (CNTs), growth on SiC and other substrate templates, substrate-free gas-phase (SFGP), and CVD[8,19]. The TD and BU approach methods to fabricate or extract graphene can vary according to their quali-

ties, equipment facilities, purity, size, scalability, among others. Table 2.2.4.1 shows the main advantages and disadvantages of TD approaches for graphene synthesis methods. Cleaving and electrochemical exfoliation provide high conductivity properties recovery, however, they are not affordable for large-scale production due to the cost of reagents like PVC for the adhesive material elimination and the cost of the ionic liquids in the electrochemical cells. Arc discharge and AFM cantilever exfoliation can produce high-quality graphene in a controllable layer but their process implies expensive equipment. On the other hand oxidative and electrochemical exfoliation results in simple procedures that made it possible for large-scale industrialization.

Regarding to BU graphene synthesis methods, table 2.2.4.2 it is shown the advantages and disadvantages among the principal. First, the pyrolysis method produces graphene with dimensions up to 10 μm, however, these may contain a high number of defects and a low quality material.[19] By unzipping a single-walled carbon nanotube is very effective for the production of graphene nanoribbons (GNRs), this process provokes the simultaneous creation of oxygen-containing functional groups in the resulting material. Substrate growth is a BU approach that offers high surface area while its main obstacle is the limitations in scalability.[9] SFGP is still a method under development that promises high possibilities for industrialization, however, one of its current challenge is the removal of defects. CVD is one of the methods that produce the best quality near-pristine graphene, however, hazard components are involved in the procedures.[19] From those, LPE, CVD, epitaxial growth, and oxidative exfoliation-reduction[8] have demonstrated to be the most convenient methods for their affordable process, high yield, and potential industrialization. Research and improvement in these fabrication methods must continue to obtain graphene with highly manipulable properties and so be integrated in the industry for the near future. Graphene oxide resulting from the graphite oxidative reduction method is the main interest in this work.

The principle work of the LPE is to weaken the van der Waals forces between the graphene layer, either for intercalation or functionalization, by dispersing graphite in a solvent medium, in this way, it is possible to have enough surface energy to overcome the interlayer forces. The solution is then exfoliated by sonication or ball milling. For this method to be highly favorable, the accurate selection of the solvent has to be carried out. It can be divided into three different categories according to the medium selected: organic solvent-assisted exfoliation, surfactant-assisted exfoliation, and other exfoliation methods.[8] The average thickness obtained in this method about 6 to 7 layers. Simple procedure, high-volume, low cost production and

Table 2.1: Advantages and disadvantages of graphene top-down synthesis techniques

Technique	Advantages	Disadvantages
Cleaving technique	Controllable, high quality, large size and unmodified graphene sheets.	Very small scale production due to cost of adhesives such as PVC and the purification from the adhesive.
Arc discharge	Moderate scalability (produces ~10 g/h of graphene with a number of layers between 2 to 10).	Low quality and carbonaceous impurities. Expensive due to vacuum or pressure equipment.
AFM cantilever exfoliation	Moderate production of few layers.	Large thickness, about ~10 nm, comparable to 30 sheets of graphene.
Sonication or LPE	Uses environmentally friendly chemicals. Inexpensive. Good for trading and industrial implementation.	Separation and defects on its edges and basal planes (some of them can be avoided).
Electrochemical exfoliation	Single-step functionalization and exfoliation; high electrical conductivity of the functionalized graphene.	Cost of ionic liquids.
Oxidative exfoliation	High-scale production and low cost.	Low surface area, poor electronic conductivity and some permanent defects during the oxidation process.

high quality resultant graphene make of this method one of the most successful for obtaining of graphene. However, since common solvents used are not volatile, it implies an extra step for the removal of the residuals.[25] Unfortunately, in this removal process, the graphene layers tend to re-stack, which is a great disadvantage. Graphite powder was dispersed and sonicated in organic solvent N-methyl-pyrrolidone (NMP) to obtain colloidal suspension of graphene sheets by Hernandez et al.[20] It produced graphene dispersions with concentrations up to 0.01 mg ml^{-1} because of the high match of energy surfaces between solvent and graphene. These dispersions

Table 2.2: Advantages and disadvantages of graphene bottom-up synthesis techniques

Technique	Advantages	Disadvantages
Pyrolysis	Dimensions of up to $10\,\mu m$	Low quality. A high number of defects.
Unzipping CNTs	Size controlled by selection of the starting nanotubes.	Expensive starting material; oxidized graphene.
SiC and other substrates growth	A very large area of pure graphene.	Very small scale.
Substrate-free gas-phase	Production of 2 mg/min with high quality. High scalability and commercialization.	The method under development. Requires morphological characterization and removal of defects.
CVD	Large size; high-quality uniform layers	Chemical hazards.

can then be used to deposit flakes by spray coating, vacuum filtration or drop-casting. They also reported that in the removal process of NMP residual, it could not be completely removed and, after room temperature drying and annealing process ~ <7 wt% remained.[20] Their work opens the possibility of sensor applications based on graphene electrodes.

BU approach CVD method consists of a thin film coating process and is a very fundamental method for much of the electronics of today. The precursors, which in this cases, are hydrocarbon gases (such as methane (CH_4), acetylene (C_2H_2), ethylene (C_2H_4), and hexane (C_6H_{14})), that gets thermally induced in a vacuum chamber until vaporized and then deposited at the substrate's surfaces, generally metals.[8,58] Temperature is the control parameter for this method. For the growth of graphene in SiC, low temperatures are used to limit the diffusion of the Si atoms from the SiC crystal depth.[58] One important advantage of this technique is the potential industrial-scale production of graphene. Besides, it produces high-quality and large-size graphene. One important disadvantage is the high temperature required that can damage the substrate and the graphene. The temperature for graphene to grow varies depending on the precursor, e.g. CH_4 at the gas reaction of 10 standard cubic centimeters per minute (sccm) and nickel as the catalyst

(substrate), requires 1000 °C. For this case, graphene thickness results in 1, 2, and multilayered graphene. For a copper foil of 206 nm thick and as precursor H_2/CH_4 at 5 sccm, the temperature was 800 °C for 1, 2, and 3 layers of graphene.[59]

The epitaxial or substrate growth method is a high-temperature treatment, about 1200 to 1600 °C, which deposits a single crystalline film of graphene on a single crystalline substrate, generally Si, since its crystallinity matches with the substrate and its melting temperature is 1100 °C.[8,19] The process is carried under inert gas or vacuum conditions. According to Norimatsu's group epitaxy growth of graphene on SiC is the best choice as it creates a homogeneous growth and allows a and the carrier mobility reaches as high as several m^2 V s^{-1}. The addition of a buffer layer like a carbon layer which periodic structure grew on SiC face displacea the carbon atoms. Then the broken layer cannot further be called graphene since it does not present a linear band dispersion and so it is not electrical conductive[19,60] On the other hand, when growing graphene on C-face, it does not grow homogeneously but in all directions on the terrace creating multilayers. Graphene on SiC has been established as a novel resistance standard based on the quantum Hall effect (QHE), demonstrating that graphene is an ideally clean two-dimensional electron gas (2DEG) system.[60]. Although the high-quality resulting material, is slow and expensive due to the energy-intensive process and limited size of commercial SiC substrate; and, it is not available for many substrates yet.[8,19,60]

Among the most convenient techniques for obtaining graphene, in terms of affordable reagents and equipment, chemical exfoliation has been reported as one of the most appropriate methods, which consists of two steps: First, it weakens the van der Waals forces to increase the interlayer space from 0.335 to 0.625 nm. Then, the layers get exfoliated by heating GO can be obtained by four principal procedures: Brodie, Staudenmaier, Hofmann, and Hummers methods.

Graphite oxide was first prepared by Brodie in 1859 by using potassium chlorate ($KClO_3$), his method consisted of an oxidation process for up to 3 or 4 days, at 60 °C, while fuming nitric acid (HNO_3); following by exfoliation in vacuum at 100 °C.[43] smaller sheet size and larger surface area. Then, in 1898, Staudenmaier proposed the addition of sulfuric acid (H_2SO_4) at 0 °C, and again KCl_3. Also, it is used HCl to remove salt ions SO_4^2, then it is exfoliated in a vacuum. Hofmann's method is based on the Staudenmaier method, the only difference is the absence of fuming. In 1958, Hummers and Offeman proposed their method which is the most widely used because of its simplicity and quickness. Hummers noted previous methods were
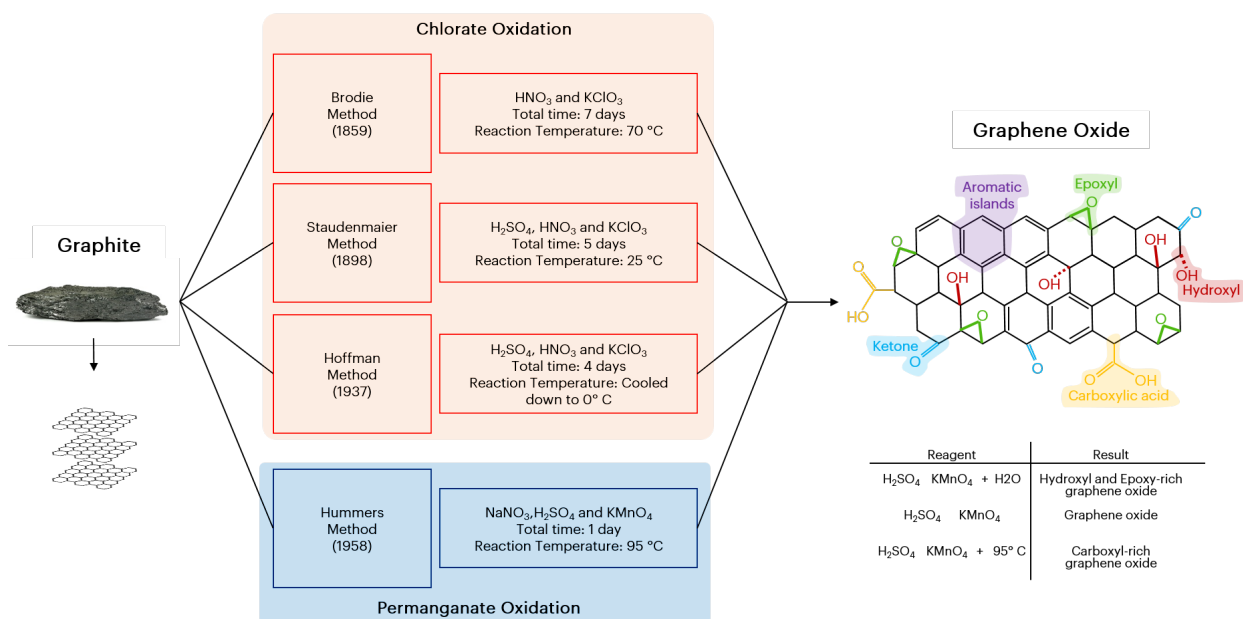
Figure 2.6: Graphite oxidation routes: chlorate oxidation and permanganate oxidation. The use of the different oxidazing agents that cause the addition of epoxy, hydroxyl and carboxylic groups, and aromatic islands in the graphene structure. Adapted from [8,63]

dangerous and time inefficient.[62] This method treats graphite with a water-free mixture of $NaNO_3$ it is cooled down with H_2SO_4, the suspension is kept to 20 °C with $KMnO_4$ and the temperature is elevated until 98 °C. While some modifications have been proposed, the main chemical reduction technique is unchanged.[62]

In the work planted by Botas et al.,[43] Brodie's method was used for the preparation of graphene structures and they stated it introduces smaller amounts of oxygen groups than Hummers method; however, it favors the formation of conjugated epoxy groups and hydroxyl, which favors the incorporation of oxygen in-plane as ether groups or out-of-plane as carbonyl groups at certain temperatures. These groups are highly stable.[43] On the other hand, different graphenes prepared by Staudenmaier, Hofmann, and Hummers methods by Poh et al.[63] and presents that graphene prepared by the Hummers showed higher heterogeneous electron transfer rates and lower overpotentials as compared to graphenes prepared by the Staudenmaier or Hofmann methods.[63] Besides, rGO synthesized from Staudenmaier, Hoffman, and Hummers methods yield

significantly different electrochemical responses. This is due to the different reagents used for the oxidation of graphite, which not only introduces different levels of oxygenated specie, but also introduces impurities, especially in the case of the Hummers method, which is purported to introduce N heteroatoms to the in the structure.[46] These functional groups also contribute to GO being hydrophilic and thus dispersive in water and other solutions such as ethylene glycol, N-methyl-2-pyrrolidone (NMP), and tetrahydrofuran (THF)[8]. Because a large number of functional groups are introduced during these procedures, the use of reduction reagents to remove them is necessary. In this work, we will start from the chemical reduction methodology, which despite not showing the best results in terms of quality of electrical conductivity of graphene, is the one that is most convenient and affordable. From this step, we will proceed to make reductions of the resulting material through reducing agents to achieve a graphene with an elevated C/O ratio.

C/O Ratio in Carbon Materials

The carbon-oxygen ratio allows the identification of the content of both elements and, consequently, to determine the state of the electronic structure. GO is a non-conductive monolayer, highly defective and highly in oxygen group content, typically characterized by a C/O ratio closer to 2:1. These characteristics are affected by choosing the proper graphitic material for oxidizing and the proper chemical method for reducing. When exploiting the distinctive conductive properties of graphene to build electrochemical sensors, energy storage devices, transparent conductive films, and others, the abundance of functional oxygen groups added to graphene also provide an interesting redox activity since these can be removed or added to the structure, facilitating the transfer of electrons for sensing devices. For biosensors, carboxyl and oxygen-containing functional groups provides a covalent attachment of biorecognition molecules.[42] However, the abundance of oxygen functional groups provide GO with an inherent redox activity, as some of the oxygen functional groups can be reduced and regenerated electrochemically. This allows GO to be exploited as a signal carrier in certain electrochemical sensing schemes. On the other hand, chemically reduced graphene materials can be used as transducer materials in electrochemical devices due to better electrical properties, a high density of defects, and edgelike planes, which facilitate fast electron transfer. Moreover, well-defined graphene oxide platelets (defined by dimensions of the nanofiber base) that can disperse as colloidal solutions can be fabricated from the oxidation of graphite nanofibers.

2.3 Reduced graphene oxide (rGO)

Graphene oxide (GO) obtained from the oxidative exfoliation of graphite oxide has an almost identical chemical structure as graphene.[36] However, GO has a high content of oxygen functional groups which changes many fundamental properties in the material, especially its conductivity. Efforts to obtain a material closest to pristine graphene as in mechanical exfoliation have been enormous. GO can form stable aqueous colloids in simple solutions due to its hydrophilic nature[55]. Finally, GO can be easily reduced by different methods (chemical, thermal and electrochemical) to produce a material closer to pristine graphene, resulting in reduced graphene oxide (rGO). The conductivity properties of graphene rely in the mobility of the π-electrons. By treating GO with reducing agents it is possible to restore its electrical properties. These reducing agents lose or donate electrons in a redox reaction, allowing the oxygen groups to be removed from the compounds. Principal reagents hydrazine (N_2H_4),[64] borohydrides (sodium borohydrade ($NaBH_4$), sodium cyanoborohydride ($NaBH_3(CN)$) and sodium triacetoxy-borohydride ($NaBH(OAc)_3$),[12] aluminum hydride,[65] hydrohalic acid,[66] sulfur-based reagents,[67] nitrogen-based reagents,[68] metal-acid,[69] metal-alkaline.[70] As well as green reductants like sugars,[71] plant extracts,[72] microorganisms,[73] and proteins,[74] and amino-acids[75] have been explored. Each reducing agent can cause numerous defects in the original honeycomb lattice, by creating holes, introducing additional atoms, or provoking a reorganization of the carbon lattice, such as five-membered rings. $NaBH_4$ has been widely studied since demonstrated more-effective function than hydrazine as a reductant for GO,[12,19,28] which chemical reduction results in 6.87 for C/O ratio in 24 h process.

2.4 Electrochemistry

The field of electrochemistry makes it possible to identify all the phenomena involved in the transfer of electrons,[57] process that, in other words, is the main reference of the flow of electrical conduction. In inorganic chemistry, the resulting chemical change is often the oxidation or reduction of a metal complex.[57]

2.4.1   Three-electrode electrochemical cell configuration

Two types of electrode configuration can be assembled: two-electrode configuration, used in i.e. gas sensors, and three electrode configuration. The three electrodes are: working electrode (WE), reference electrode (RE) and counter electrode (CE).[57] The quality of these electrodes systems can be envisaged according to features like sensitivity, selectivity, reversibility, response time, and long-term stability.[57]

Working electrode is where the electrochemical reaction of interest is occurring. WE consist in a redox-inert material which is connected to a potentiostat for control the potential to be applied.[57] Since surface of the WE must be clean and surface-are well-defined, they are commonly made of materials such as inert metals like gold and silver, and inert carbon such as glassy carbon, boron doped diamond, and mercury drop, platinum, and film electrodes. In case of impurities in the WE, these are removed by a sonication treatment in ultra-purified water.[57] There have been created functionalized electrodes for the proper analysis of organic and inorganic samples.

Reference electrode is the reference point which will determine the potential of the electrochemical cell since it has a stable equilibrium potential.[57] A accurate RE remains invariant during the monitoring of the potential of a reaction. Some example of RE in a cell is calomel electrode consisting in Hg/Hg_2Cl_2, or also, silver/silver chloride electrode containing Ag/AgCl. Both electrode types are in contact with a concentrated KCl solution. The electrodes are separated by a porous material from the solution.[57]

Finally, the counter electrode, also known as auxiliary electrode, and which purpose is to complete the electrical circuit and establishes the electrical potential flow between WE and CE. In this way, an electroanalytical study from the cell can be obtained from applying or measuring a current between both electrodes. Alone, processes occurring in CE are ignored in general. Then the potential is not measured but adjusted so as to balance the reaction occurring at the WE. Counter electrodes can be made of inert materials.[57]

2.4.2   Optical Fiber as Working Electrode

When designing nanosensors, the use of OF, that have traditionally been used for the transmission of a light source with the lowest loss, are now implemented to meet its basic features like flexibility, chemically compatible for the composite material, and electrical passivity. The transmittance
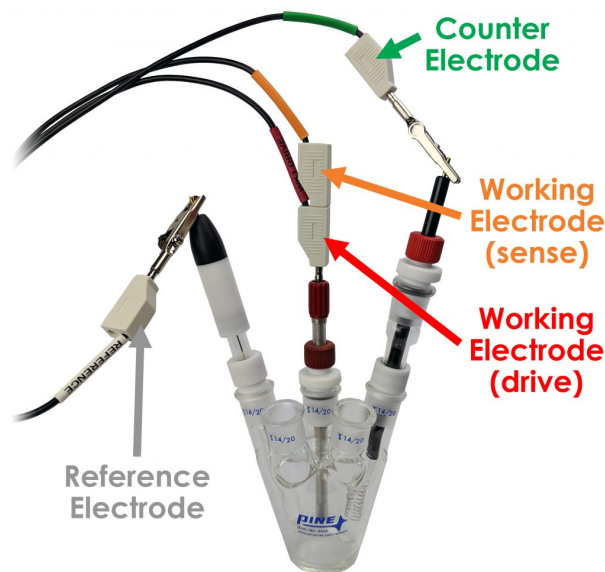
Figure 2.7: Typical three-electrode cell configuration. Adapted from[53]

of a material is mainly determined by its electronic structure. For example, glass is transparent because it is an insulator with a large bandgap. OF is generally fused silica. OF-based sensors can be divided into two categories. The first one is called an extrinsic sensor. OF consists of two principal parts. On the inside, it have a core made silica (plastic in some cases) that allows internal diffraction of the light signal that travels along, and is about 8 μm in diameter (typically measurement is single-mode types). At the outside, it has a cladding with a diameter of about 125 μm and which is commonly made of silica. This section has a lower refractive index and its purpose is to reflect back the light towards the core. For communications, a polymeric coating buffer surrounds the cladding and a jacket that protects the cable from external conditions such as temperature increases or solvent contacts. As only the OF core is the material of interest, the methodology used to remove the polymeric coatings and other organic components will be explained in detail later. In Figure 2.8 a) a representation of the structure of OF is shown, in which the different polymeric layers that cover it can be observed to allow its functionality, as mentioned above. On side b) you can see the reference samples used in this project. Once OF was stripped of all coatings and coated with rGO.
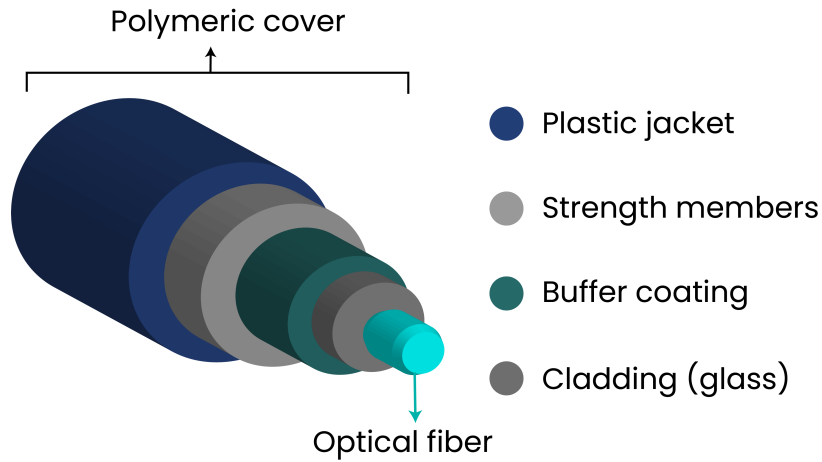
Figure 2.8: Optical fiber structure showing the different coatings that protect the SiO core.

2.5   Characterization Techniques

2.5.1   Raman Spectroscopy

Raman Spectroscopy is a very precise spectroscopic technique for obtaining information about the vibrational states of the molecule, and it is very used for carbon material characterization. In 1928, Sir Chandrasekhara Venkata Raman described the inelastic scattering behavior of a monochromatic light source with a certain frequency V_o. The spectra obtained consist of a pattern of shifted frequency (Raman spectrum) and the Rayleigh line. It is important to take into account that the Raman effect is a fragile process, usually, 10-8 times smaller compared to the incident radiation. An essential aspect of optical absorption by crystals is related to the wave vector conservation. Since we are working in the visible range, the wavelength of light λ_{light} is of the order of 500 nm. If we consider the dimensions of the Brillouin zone defined by the wavevector k, usually given by $k_{BZ} = \pi/a$. 100 Where a is the primitive vector of the unit cell with a value of about 0.1-0.2 nm.

$$k_{light} = \frac{2\pi}{\lambda_{light}} \approx \frac{k_{BZ}}{3000} \tag{2.10}$$

The working principle of Raman is summarizing in the incident laser wavelength that reaches the sample and from them, three types of scattering will be detected. When the monochromatic incident radiation reaches the sample, an inelastic scattering process occurs and provokes molecular vibration. Rayleigh scattering is created by the scattering radiation from the laser-sample interaction. In general, its frequency would be equal to the frequency of incident radiation. While a minimal fraction of the scattered radiation will have a different frequency and constitutes the Raman scattering. From this two bands can appear: first, when the frequency of incident radiation is higher than the frequency of scattered radiation, then it is called Stokes lines. Second, when the frequency of incident radiation is lower than the frequency of scattered radiation, it is called anti-Stokes lines. Rayleigh scattering, which is about 1 in 10^4 photons, will scatter from the sample with an angle without being absorbed and with the same frequency as the incident. Raman scattering which is about 1 in 10^7 photons will scatter from the sample with a specific angle and specific frequency.

The difference in energy $\pm\sim \omega s$ corresponds to the created/annihilated phonon. Stokes and
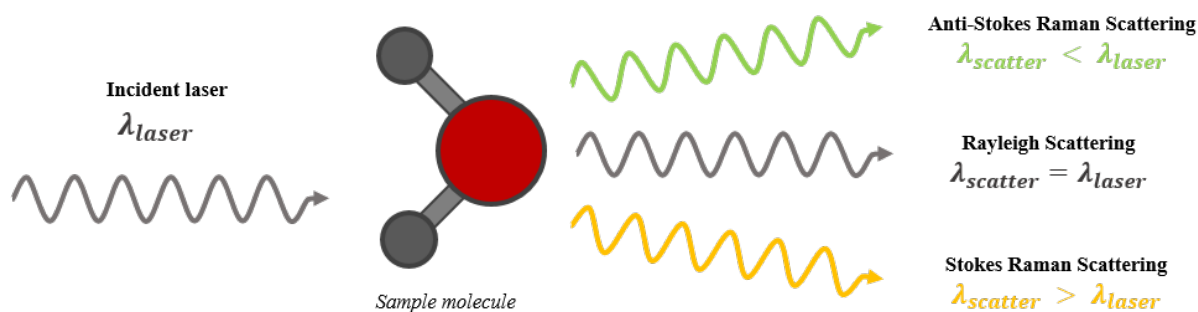
Figure 2.9: Representation of the incident wavelength that strikes in the sample. Most of the scattered light has the same wavelength as the source, it is Rayleigh scattering. Scattering with different wavelength provide elemental information of the molecule, it is Raman scattering.

Anti-Stokes scattering are two-photon events, including the annihilation of the irradiated photon and the creation of the scattered one. When the energy of the incoming or scattered photon matches the transition energy of an allowed electronic transition, the process is said to be reso-

nant. Similarly, a double resonant process is possible. In this case, in addition to the resonance condition, the excitation makes a real transition. The point mentioned before explains why the double resonant process is much stronger than single resonant processes.
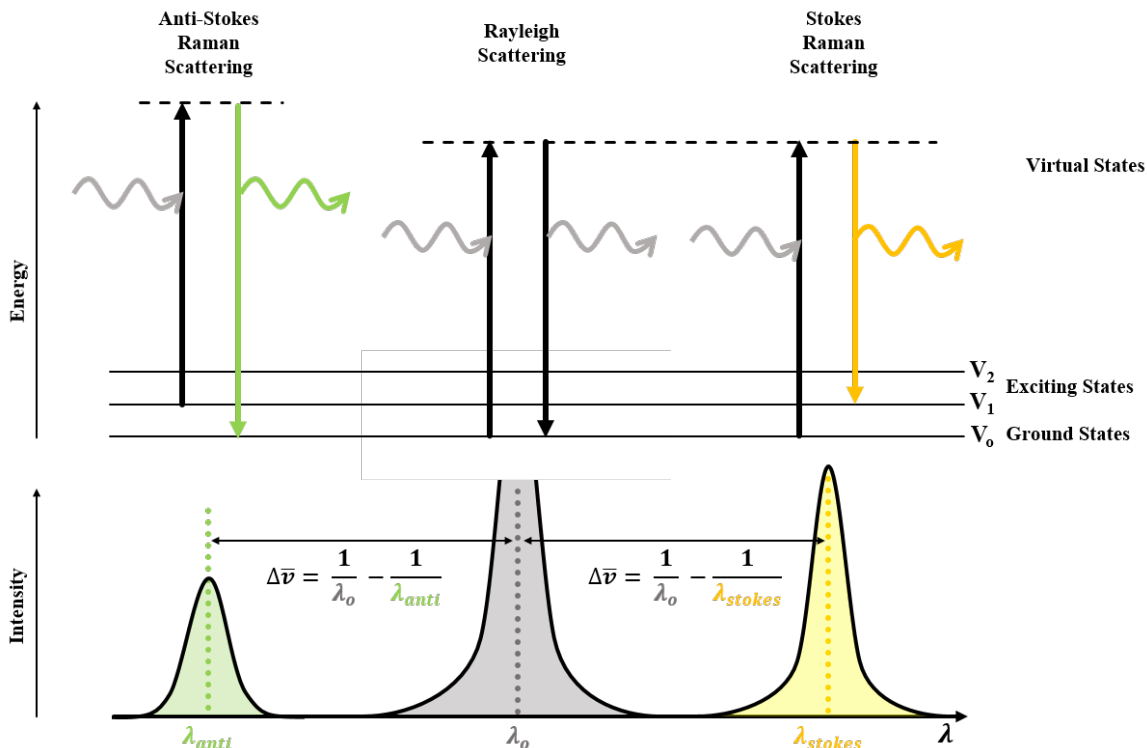
Figure 2.10: Schematic representation of the principle of Raman scattering. In green, the formation of Anti-Stokes scattering; in grey, Rayleigh scattering; and in yellow, Stokes scattering.

Raman scattering is focused on studying the scattered light but not the absorbed nor emitted, this allows obtaining information from the vibrational modes at the electronic clouds of the material under study. Particles, atoms, and molecules, are subjected to parameters that allow positioning them in a phase of a dynamic system. A particle has been given $3N$ degrees of freedom (DOF), where N is the number of interacting atoms in the molecule. This behavior includes molecular translational, rotational, and vibrational motion. In this case, nonlinear molecules, three of these DOF correspond to movements of the center of mass in x, y, and z-axes

(for a 3D spatial motion); likewise, three DOF are associated with the rotational motion at these same axes. The remaining DOF describes the molecular vibrations that produce a change in the interatomic distance or a change in the angle of the chemical bonds involved. A normal vibration mode can be described by the behavior of a harmonic oscillator, however, the vibrations in the chemical bonds are not harmonic and therefore their energy levels are not equally spaced, and also each one has a characteristic vibrational frequency. In Figure 2.11 the six different ways of vibrational mode are shown, they are divided into two basic groups: stretching and bending modes. Stretching vibrations represents a change in the length of the bonds, in which the motion can be symmetrical or asymmetrical. Symmetrical movements indicate a change in length in the same directions while asymmetric movements will show changes in length in different directions to the center atom. Then, within the bending modes, the movements are also classified by their position in the plane or out the plane. The vibrations inside the plane are rocking, which describes a change in angle by the movement of the atoms in a synchronized direction; and, scissoring, which describes a change in angle by the movement of the atoms in a des-synchronized direction or opposite direction. Out-of-plane vibration modes are classified in wagging, a symmetric bending mode that indicates a change in angle between atoms due to oscillation in the same direction out of the plane; and twisting, asymmetric bending mode since it involves a change in angle between atoms due to an oscillation in different directions out of the plane. The kinetic energy of the DOF does not contribute to the temperature but the specific heat of the system under normal conditions. Since each vibration has a different force constant and reduced "effective" mass, therefore the frequencies are unique and a single band position will be obtained for each molecular group, for this reason chemical analysis through the Raman spectrum is possible.

Raman Spectrometer

There are four principal components in te Raman spectrometer: the laser excitation source, the sampling chamber, the spectrometer, and the detector. Figure 2.12 represents the characterization process: inside the sample chamber, a monochromatic laser source, which is energetic and narrow, passes through an optical path and excites the sample to obtain radiation. The optical arrangement is composed by a beam splitter that dissociates the monochromatic laser source into two different directions: the anti-Stokes signal appears in the opposite position relative to the Stokes signal with respect to the central Rayleigh signal.[40] Before the light gets into the spectrometer, Rayleigh
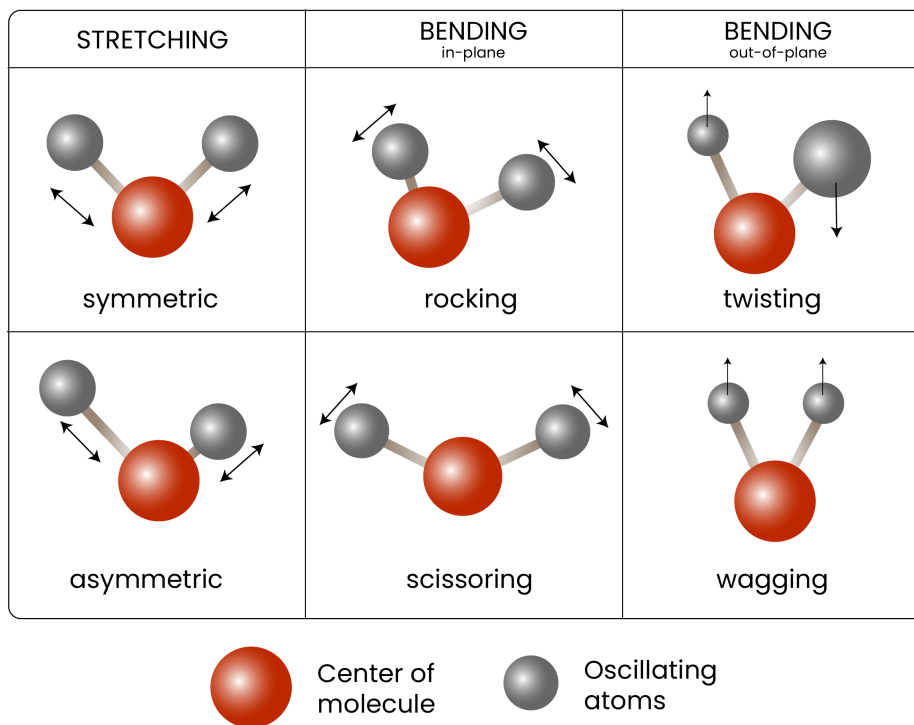
Figure 2.11: Vibrational modes for non-linear molecules 3N-6 DOF sorted according to the change in interatomic length (stretching modes) and change in angles between the atoms (bending modes), and, by symmetric or asymmetric transformations, inside and outside the plane, which have unique frequencies that position the bands in the Raman spectrum.

signal has to be eliminated by using a filter, for this a combination of a bandpass filter and a notch filter is used to isolate the beam. Other devices use two or more filters, gratings, and monochromators (such as super notch filters, rejection filters, holographic notch or edge filters, and holographic filters)[52] to properly collect a well-defined scattering radiation. By using lenses, the beam is focused on the spectrometer through a slit and directs the divergent beam to a concave mirror, which distance is the same as the focal length of the mirror. The reflected rays are perfectly parallel a focused to the infinite (no divergence), it is said to be collimated. Then, a grating or a prism is used for reflecting and spreading out the light into different directions, from this a constructive and destructive interference are created, this is the case of a Raman dispersive

spectrophotometer. A non-dispersive Raman spectrophotometer will not diffract the light and would use an interferometer. Finally, the beam gets to a charge-coupled device (CCD) array and reads out any charge change in the pixel array. Behind, the established equations will calculate a spectra for the different energies associated with their intensities. Within the Raman spectrum, the wavelength of a phonon corresponds to 2π cm and its energy is presented in units cm^{-1} (while not in nm^{-1} due to it is a very small number). Then Raman spectra are presented as a record of energies units of cm^{-1} wavelengths from 10 to 4000 cm^{-1} correlated to their intensities, including amplitudes and displacements of the phonons due to the vibrational modes, in arbitrary units.
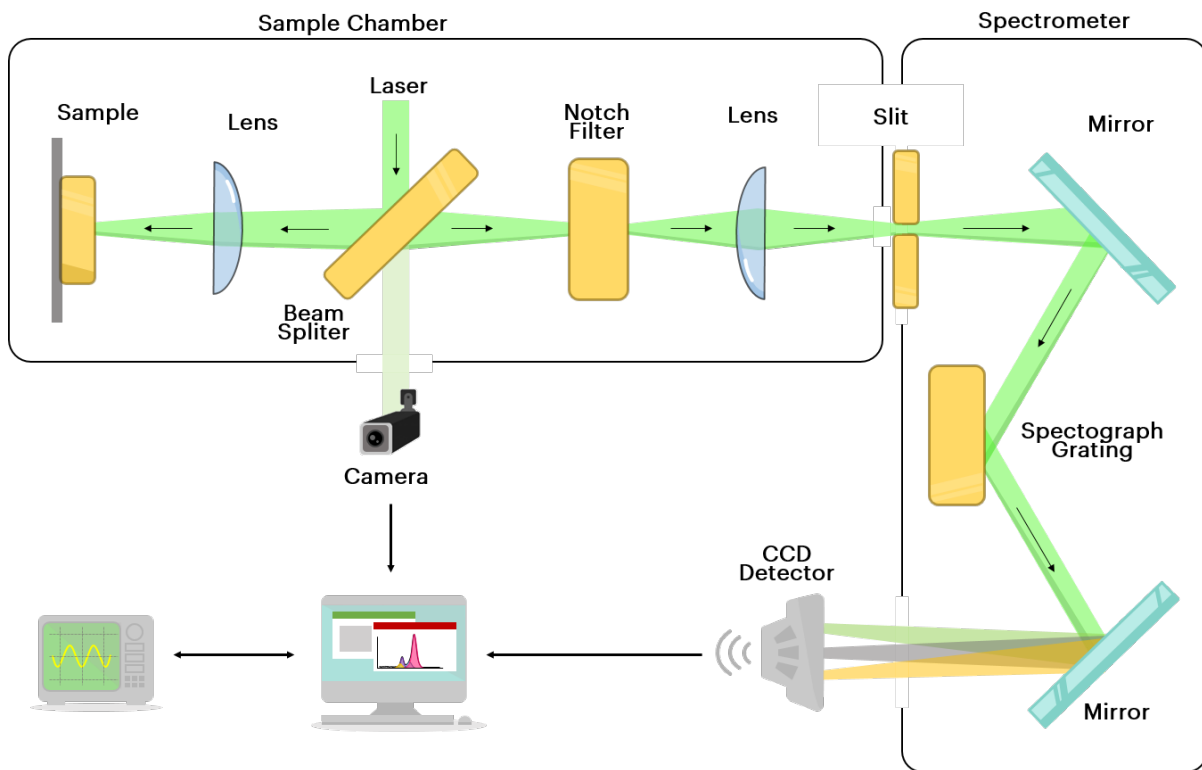
Figure 2.12: Spectrometer structure

2.5.2   Raman characterization for graphene and rGO

Raman spectroscopy has been intensely used for carbon-based materials because it allows evaluating the properties of graphene without causing damage; also, it is a rapid technique for obtaining principal information like the number of layers, doping and defect density, strain, thermal properties, and edge chirality. Raman spectrum for graphene shows its main peaks around 1580 cm^{-1} (G peak), 1350 cm^{-1} (D peak), and 2700 cm^{-1} (2D peak).[37] The first one is the distinctive peak among carbon structures like graphite, amorphous carbon, and carbon nanotubes; while the D and 2D peaks can differ according to the disorder and number of layers in the system. The narrowness, intensity, and change in frequency of these peaks are some particulars that can be answered by studying its phonon dispersion. The energies of phonon dispersion in the two atoms that form the unit cell of graphene are responsible for the major peaks observed in the spectrum and can be found at Γ, and M of the first Brillouin zone. Three acoustic (A) and three optical (O) phonons, four of which are in-plane (i) and two are out-of-plane (o). They can propagate in the known modes: longitudinal (L) and transversal (T). Knowing this, iTO and iLO have the most highly dispersive energies that contribute to the important Raman bands.[38]

G Band

The G band contribution is originated from i-phonons at Γ of the Brillouin zone. This band is very sensitive to the sp^2 C-C stretching modes and so it is to the number of layers present independently of doing.[37,38] The G band originates from the recombination of an incident photon with an electron-hole pair which have been scattered by in-plane phonons with a very short momentum. A shifted position towards lower or higher wavenumber values can represent an addition or reduction in the layers, correspondingly. As shown in Figure 2.13, according to Perumbilavil et al,[44] the G peak position corresponds to 1597 cm^{-1}, 1607 cm^{-1}, and 1595 cm^{-1} for graphite, GO, and rGO, respectively. G band shift can take place when doping, in GO for example with oxygen-containing groups. Oxygenation of graphite and graphene results in an increment of the wavenumber (G band shifts to higher frequency) due to the presence of more sp^2 C-C interactions. The intensity of G band has a linear increment in the intensity when more layers, hence sp^2 bonds increase in energy making the vibrational frequency of the bonds also increase. Finally, the G band shifts to higher frequency (wavenumber) at the Raman spectrum also increases. However, in Figure 2.13 it is observed GO has a higher shift, about 10 cm^{-1},
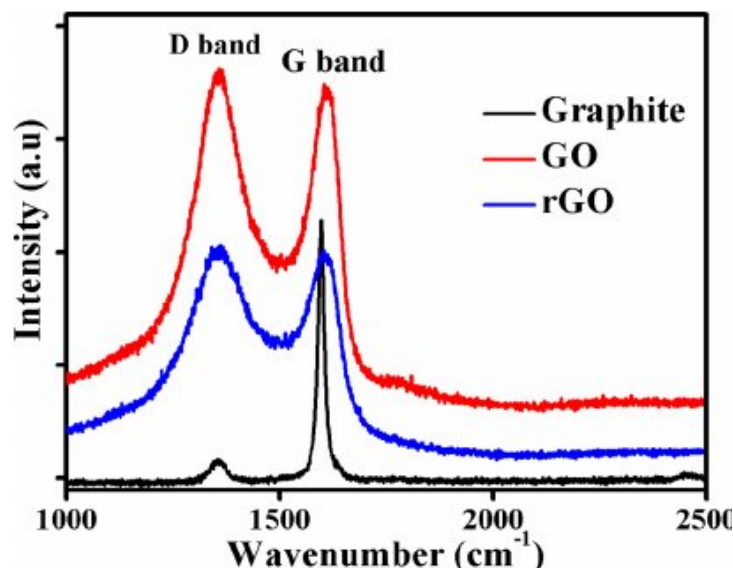
Figure 2.13: Raman spectrum comparison of rGO at 1595 cm^{-1}, GO at 1607 cm^{-1}, and graphite at 1597 cm^{-1}. Oxygen-content evolution in G band shifting can be observed. The intensity and FWHM data of G band provide information about p- or n-doping. Adapted from Perumbilavil et al[44]

for graphite. By analyzing G band to determine doping or the number of layers in GO or rGO, it is more accurate to take into account its intensity and FWHM, not only its shifting.[37] Tang et al.[37] also refers to experimental procedures of other authors comparing Raman spectrum of graphene and graphene monolayer deposited in SiO substrate, resulting in 1580 cm^{-1} (red-shift) and 1587 cm^{-1} (blue-shift) positions for G band respectively, as it can be observed in Figure 2.14. Likewise, a difference of four times its intensity can be observed at 2D band, between 2650 and 2700 cm^{-1}, this change will be deeply detailed in the 2D band section. Peaks were fit with Voigt profile functions. Both 2D and G intensity peaks are directly related to doping levels. The G band broadness origin is subjected to the electron-hole pair generation. From Figure 2.13 and 2.14, it can be appreciated a more narrow G band when more sp^2 bonds are present. In Figure 2.14, for the suspended graphene sample the mean value doping-level is less than 2×10^{11} cm^{-2}.[37] For SiO substrate supported graphene, blue shift, G band broad is proportional to the doping-level. An anisotropic strain, from the interaction of the graphene with the substrate, for example, would lead to a splitting of the G band.[37] G band is a two-times degenerative phonon at the Γ point, that

belongs to E_{2g} optical mode which splits into G^+ and G^-, transverse and longitudinal motions, correspondingly.[40] One polarized parallel to the strain and the other polarized perpendicular to the strain.[37,38] The split increases when the strain increases; for this reason, the width of the G band can determine the deformation and strain on the sample.[38] Any substrate strain could result in electronic and optical properties of graphene modification.
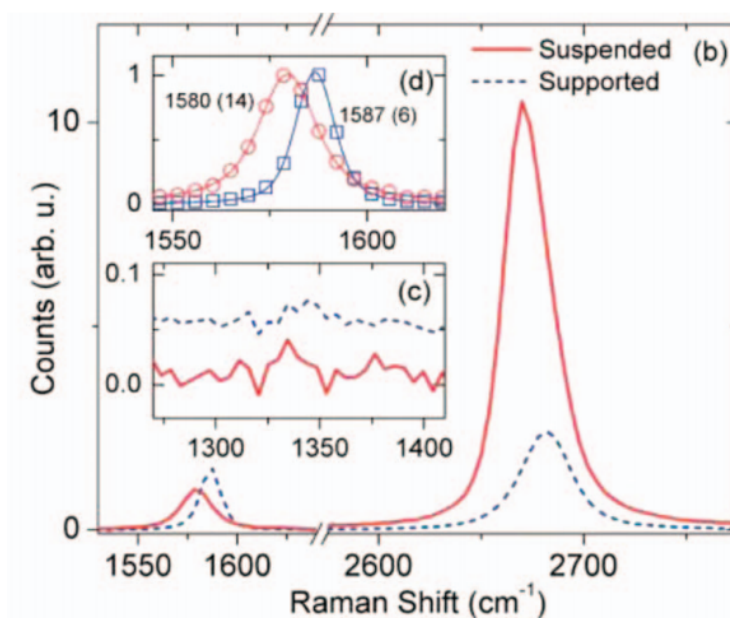
Figure 2.14: G and 2D band Raman spectrum comparison of graphene suspended and SiO substrate supported graphene in 1580 cm^{-1} (red circles) and 1587 cm^{-1} (blue squares), according to Tang et al.[37]

2D Band

The 2D band, also known as G' band, is present at 2700 cm^{-1} and it is the strongest peak, which together with the G band, exhibits the signature of all sp^2 carbon materials. Besides, in graphene, the 2D band is more intense than the G band. It is a second-order scattering process resulting from a double resonance where an electron-hole pair is created by an incident photon near the K point. The electron gets inelastically scattered by an iTO phonon to the K' point and then the

electron is scattered back by a second iTO phonon to K point because of energy conservation. The 2D band process can also be triple resonant. It is very sensitive to the excitation laser used and small changes in both the electronic and vibrational structures and acts as a probe for electrons and phonons and their uniqueness in each distinct sp^2 nanocarbon. As it was described before, by describing Figure 2.14, the shape (shift, intensity and FWHM) of the 2D band helps to describe the type of doping in the graphene material. Unlike G band shifting to higher frequencies in Raman spectrum for either n- or p-type doping, shifting in 2D band occurs as following: to higher frequencies when hole doping (p-doping) takes place and lower frequencies when electron doping does (n-doping).[37]

When identifying the number of layers in graphene, the broadness of the peak is certainly a an aspect to analyze. As shown in Figure 2.15, single-layer graphene provides a defined peak for the 2D band below 2700 cm^{-1}, as the number of layers increases the curve becomes wider and splits into four peaks of Lorentzian components; also, a shift to higher frequencies is produced. This suggests that when it exists a strain coefficient 2D band will report a blue shift, as the G band also does. Low wavenumber shifts will be experienced in the presence of tensile strain, improvement of crystallinity of the graphene or thermal expansion can be interpreted as an elongation of the C-C bond. The value of the ratio of 2D Band to G Band I_{2D}/I_G is another characteristic to identify the doping level in the material. It decreases with increased doping level and is sensitive to doping even under low doping level, for this reason, graphene can potentially be integrated into sensing devices. Although, other authors have used this ratio to identify the number of graphene layers, there is not a strong relationship with it but rather with the substrate.

D Band

The origin of the D band occurs through a second-order process and appears only when there is a breaking of the sp^2 symmetry lattice of graphene. The D band is present at 1350 cm^{-1}, and its name stands for its strong correlation with the disorder. Unlike the G or 2D bands, the D band requires out-of-plane vibrations, which are present with lattice distortions and other defects, for momentum conservation. The peak in the spectra grows proportionally to the level of the defects; in this way, graphite or multilayer graphene shows a more intense peak while graphene lacks this peak in the Raman spectra. It is related to a double resonance process. The process occurring behind this band is an inelastic scattering of an electron by an in-plane phonon near K point to K'
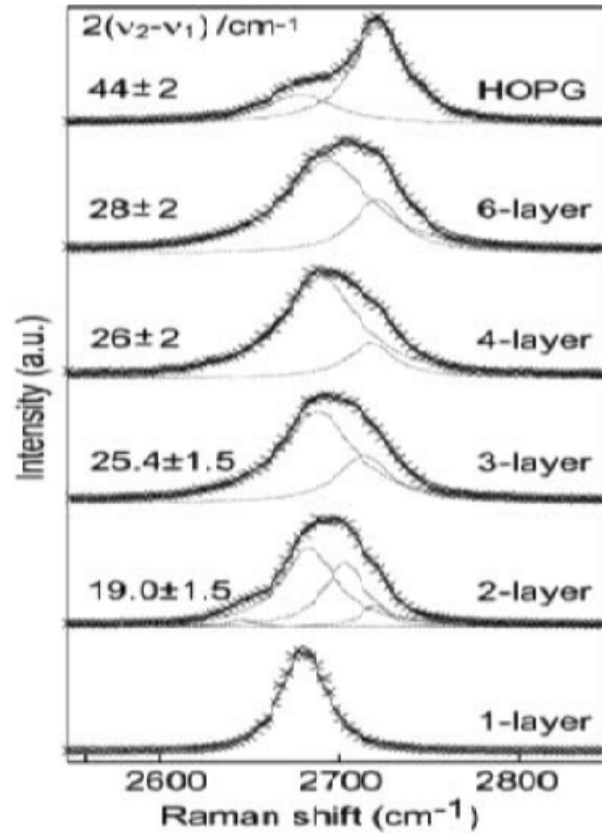
Figure 2.15: Raman spectrum of the 2D band evolution in graphene as more layer are added (from bottom to up), a blue shift is experienced. For each sample 2D band changes in intensity, broadness, and shifting. Adapted from Tang et al.[37]

point, then it gets elastically backscattered to the K point. The size of this band will be half of the 2D since only one iTO phonon participates, and its position and intensity are strongly dependent on the laser excitation, generally, energies of 2.41 eV, used for the analysis. Edge chirality can be determined by the D band, since its formation will depend on the phonon scattering being caused by two non-equivalent Dirac cones. In this way, in zigzag edges band D has a low intensity, and, on the contrary, in armchair edges band D will have higher intensity. However, it is hurried to ensure this since other factors such as laser polarization must also be taken into account.

Ratio I_D/I_G
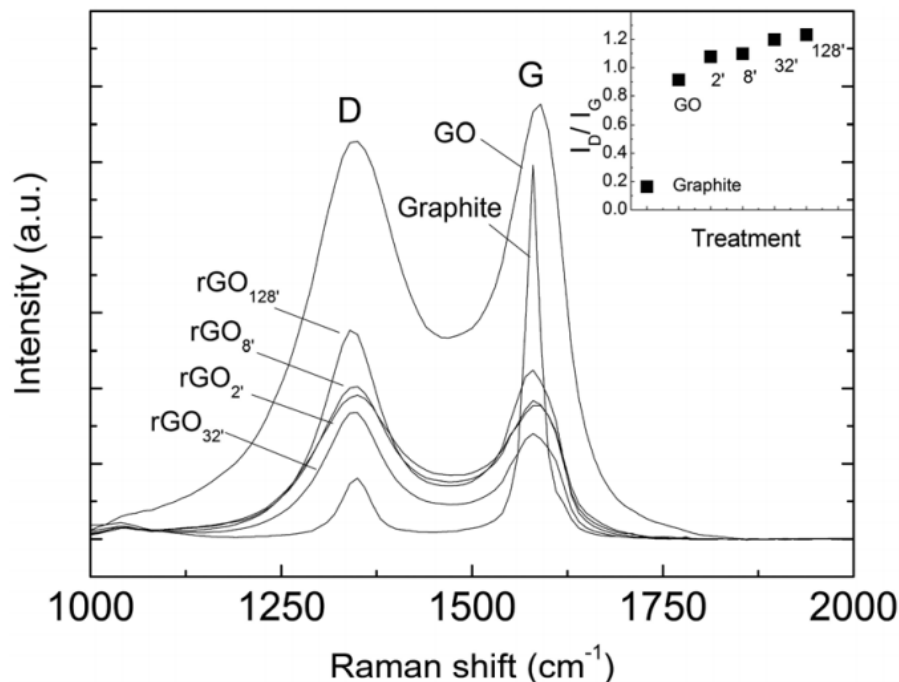
Figure 2.16: Raman spectra from the main reference article used in this work. It shows the Raman characterization of pristine graphite, pristine graphene oxide and samples of rGO in the different reduction times (2, 8, 32, and 128 min) when treating them with sodium borohydride (NaBH$_4$) as the reducing agent. The excitation wavelength used was 514.5 nm. Adapted from [12]

In the presence of disorder and impurities, the I_D/I_G ratio increases as the number and/or size of the sp^2 increases. I_D/I_G starts to decrease for sp^2 carbon hexagonal structure starts to disappear. In Figure 2.13 the Raman spectrum of the evolution of graphite, GO and rGO can be observed. For a graphitic material, the D band is almost imperceptible due to the conservation of the lattice structure, as a result, the I_D/I_G ratio will be close to 0. Thus it can also be observed in Figure 2.16 that throughout the treatment to recover the electrical properties of graphene, the radius I_D/I_G increases indicating the restoration of sp^2 lattice. A study presented by Jorio et al.[39] about the measurement of disorder in graphene by analyzing the G and D bands, describes that for a long time I_D/I_G ratio has been analyzed for the consideration of disorder in graphene. However, he indicates that it is also necessary to take into account the integrated areas of the G and D bands

(A_D/A_G). Jorio et al. examined full amorphization evolution for single-layer graphene, where it was concluded that there was an increase in I_D/I_G ratio for increasing disorder up to a point where the average distance between defects (L_D) reached about 4 nm, as well as the results for A_D/A_G ratio exhibit similar behavior. For L_D < 4–5 nm results varied strongly[39]. Finally, it was concluded that both parameters are useful for the determination of disorder (when L_D > 4 nm), but for practical reasons, I_D/I_G ratio has been used historically.

Functionalization will also change the electrical conductivity and other properties of graphene due to the interactions of more or fewer electrons in the group of molecules added. Graphene can be functionalized by electric field or chemical species; however, oxidation is the most common type of functionalization. For example, in a study on the effect on the physical and electronic properties of graphene after its functionalization with oxygen and nitrogen, carried out by Alexander J. Marsden et al.[31] shows a significant change of up to 5 atomic percent. Both oxygen and nitrogen were used in their atomic form and the results were analyzed with X-ray Photoemission Spectroscopy (XPS), Transmission electron microscopy (TEM) and Raman Spectroscopy. Only the Raman results will be discussed in this work.[31]

Raman spectra of the resulting functionalization are shown in Figure 2.17. The graph shows the G and D bands of pristine graphene, both for its exposure with a) atomic nitrogen and b) atomic oxygen. G band is shown acute while D band is not present. When graphene was exposed to nitrogen, the D band appears and widens as the exposure time to the element increases. This is how the D' peak, also called 2D, appears and in the 120 s of exposure to N, it merges with the G peak. On the other hand, functionalization with atomic oxygen for 60 s, while G band keeps narrow, D band makes its appearance after this exposure. It can be noted that this exposure had a higher level of functionalization than the sample exposed at N for 120 s. For both types of exposure, graphene 2D peak rapidly reduced in intensity and broadened. Finally, O functionalization keeps the Fermi energy at the Dirac point (undoped), while N showed a shift down in energy and the bottom of the conduction band indicating an n-doping. Results show the dominant electronic effect for both being a transition from delocalized to localized states, and hence the loss of electronic structure of graphene.[31]
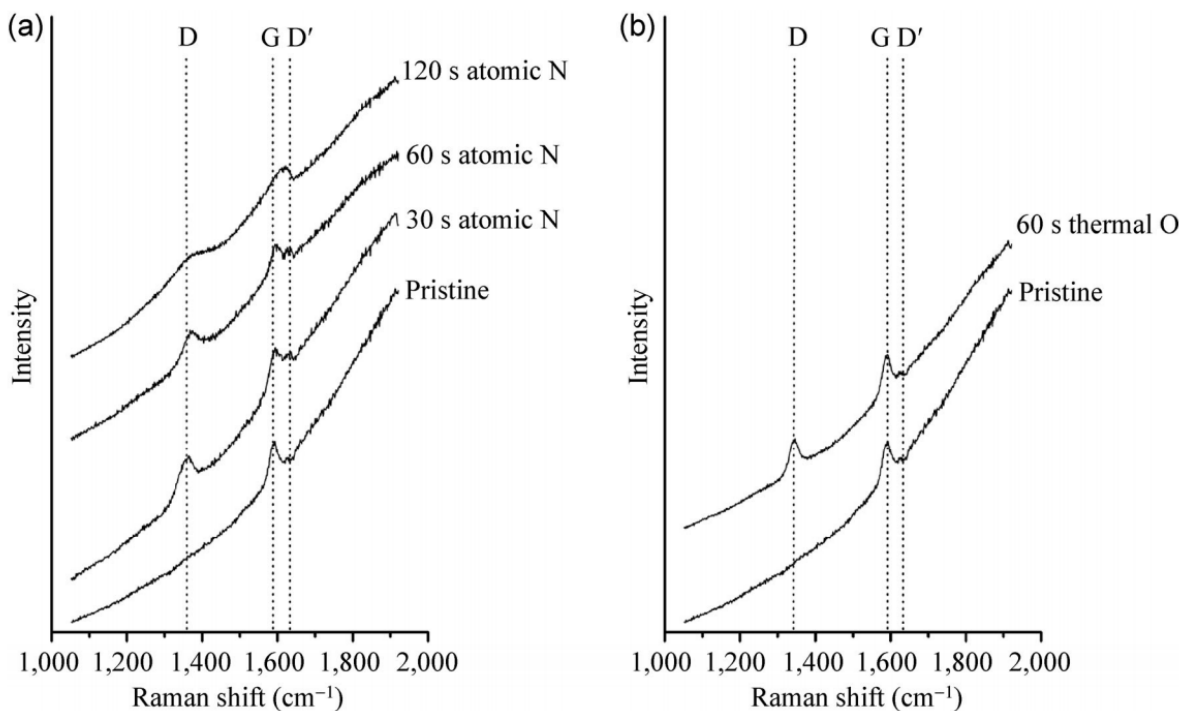
Figure 2.17: Raman characterization, centered on D/G region, of pristine graphene grown on copper foil functionalized with a) atomic N and b) atomic O, in the different exposure times. Laser excitation used was 514.5 nm. Adapted from Alexander J. Marsden et al.[31]

2.5.3 Scanning Electron Microscopy

The scanning electron microscope (SEM) produces images by targeting a beam of electrons that interact with the sample and produce an image from the emission of backscattered and secondary electrons. Inside the SEM, electrons are produced by an electron gun at the top of the column, then accelerated up to an energy of 0.1-30 keV. Then electrons pass through a combination of electromagnetic lenses (condenser and objective) and apertures to produce a focused beam of electrons that hits the surface of the sample. The objective lens aperture angle enables control the final probe size for obtaining sharper images and reduced possible aberrations. The sample is mounted on a stage in the chamber area and, unless the microscope is designed to operate at low vacuums, both the column and the chamber are evacuated by a combination of pumps. The

level of the vacuum will depend on the design of the microscope. When the electrons scatter from the sample and retain their kinetic energy until the end, then the process is said to be an elastic scattering, these electrons are backscattered. If the atomic number in the chemical composition of the sample is high, then the probability of elastic dispersion processes increases. This is because the effective nuclear charge decreases for electrons in the outermost orbitals. On the other hand, in the scanning process, the main beam transfers energy to electrons in the sample, enough to be excited and leave the sample. They are considered secondary because they come from radiation generated by the main electron beam. This process is an inelastic dispersion, which in samples with a lower atomic number chemical composition are more likely to be carried out. Secondary electrons provide key information about the topography of the sample surface. Secondary electrons have less energy than the backscattered electrons. The final result is rich in information about the chemical composition and surface topography of the material through an image. For the development of this thesis, SEM micrographs were taken with X-Ray Photoelectron Spectroscopy (XPS) PHI Versa ProbeIII (Physical-Electronics) equipped with SEM Microprobe that provides scanning X-ray induced secondary electron images (SXI) generated by scanning a focused sub -10 m X-ray beam across the sample. In this way, SEM was not a piece of isolated equipment but an additional instrument inside an x-ray photoelectron spectroscope; only secondary electrons were the carriers for topographic information but not backscattered electrons. Samples were prepared in a carbon substrate and the characterization was performed under a high vacuum.

Figure 2.19 shows the micrographs the main reference of this project which is a concentric graphene-based electrode in fiber optics produced by researchers at Lancaster University. The images were made by the secondary electron detector inside the XPS. From left to right you can see the 200 μm micrographs where one of the ends of the OF was determined as a starting point to analyze the quality of distribution of graphene along with the fiber. The OF had dimensions of 220 μm in radius and 60 mm long which were immersed in GO solutions. The first micrograph shows a non-homogeneous distribution where small clusters of GO have been created, while the upper side of the bar lacks the material. In the following micrograph with a resolution of 50 μm, it can be observed that in the spaces where GO has adhered, it presents accumulation in vertical layers. This could be understood as a multilayer graphitic material with a moderate electrical property. However, in the last micrograph, it is observed that the GO coating exposes
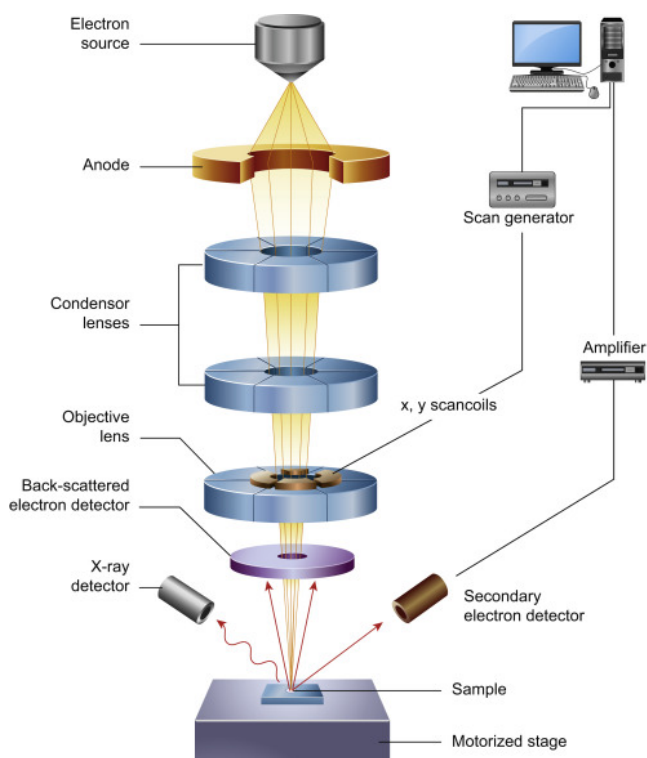
Figure 2.18: Scanning Electron Microscope structure. Adapted from [45]

the material in the form of flakes that alludes to its name, the concentric graphene ring that they manufactured. They indicate that these edges arranged in a micro-ring design allow higher sensitivity to electrochemical activity. [14]
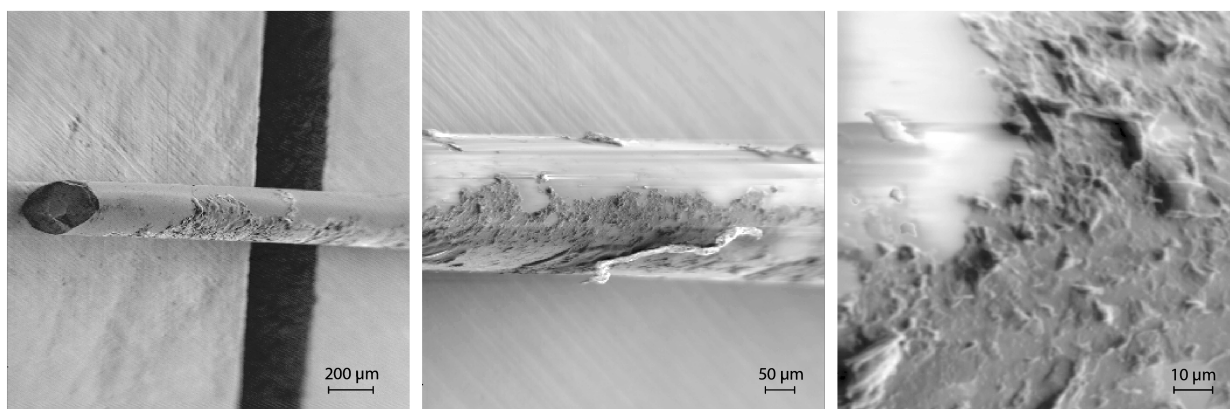
Figure 2.19: Graphene ring micro-electrode concentric to fiber optic electrode produced in Lancaster University, from left to right resolutions of 200, 50 and 10 μm.

Chapter 3

Methodology

3.1 Materials

Graphene oxide with a 0.1 wt% solid content was obtained from Abalonyx A.S. (Oslo, Norway). Reagent 3-aminopropyltriethoxysilane (APTES) 97% purity was purchased from Sigma-Aldrich (Mexico, Mexico) and purified by distillation; $NaBH_4$ and C_2H_5OH reagents and other materials were provided Yachay Tech University and were used as they were received without further purification. All aqueous solutions and washing procedures were made with ultrapure water obtained from Milli-Q® ultrapure water quality. Optical fiber was obtained from Compañia Nacional de Telecomunicaciones CNT (Quito, Ecuador).

3.2 Experimental

The process followed was:

Experimental
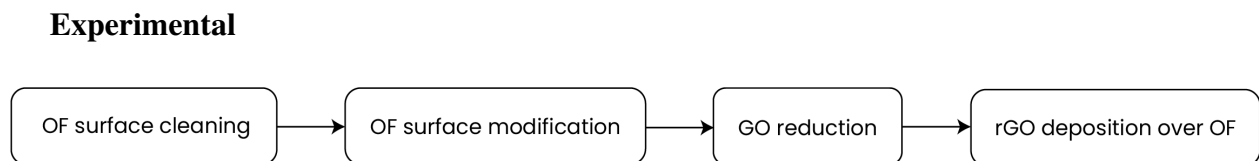
Figure 3.1: Graphical methodology.

Characterization
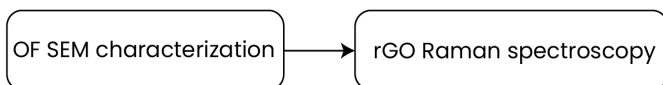
Figure 3.2: Graphical characterization.

3.2.1   OF Surface Cleaning

At first, the optical fiber comes with a polymeric covering that allows its use for the transport of information. To remove this, two methods of cleaning were used. First, oxygen plasma treatment, in which the expected results were not obtained. Second, furnace piranha solution, which dissolved the coatings.
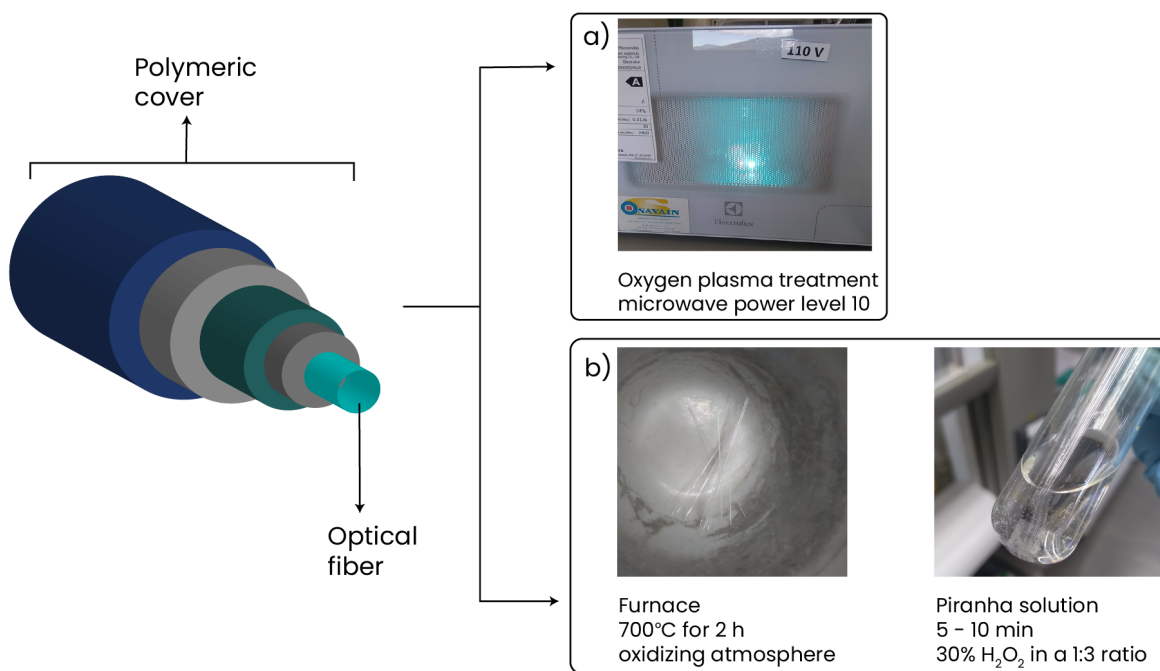
Figure 3.3: Cleaning process.

Oxygen Plasma Treatment Oxygen plasma is used to remove impurities, like organic and polymeric substances, from the surfaces before bonding. In this process, oxygen is converted in plasma into a chamber. This was performed in a standard microwave with power 10, in this way oxygen atoms get excited and ionized. A light-blue and light-purple light were obtained.

Furnace and Piranha Solution The fibers were placed in a muffle furnace in an oxidizing atmosphere at 700 °C for 2h to remove the protective coating. In a subsequent cleaning process, the fibers were submerged in piranha solution (concentrated H_2SO_4 and 30% H_2O_2 in a 1:3 ratio) for 5 to 10 min to remove any organic residue and to introduce hydroxilate to the surface. The fibers were washed with ethanol and stored in N_2.

Figure 3.4: Optical fibers immersed in piranha solution for removal of organic material.

3.2.2 OF Surface Modification

To make rGO able to get attached to OF, fibers were placed in a solution of 25 mL of ethanol, 0.5 mL of water, and 0.5 mL of APTES, in a reflux condensation process for 30 mins. Then, fibers were washed with 15 mL of ethanol and dried at 100 °C in an oven. Reflux and dry processes were repeated. Finally, the fibers were stored in N_2.

3.2.3   Reduction of Graphene Oxide

In this stage, three different methods were carried out for the chemical reduction of GO and thus recover its electrical properties. For GO reduction, a modified method reported by Guex et al.[12] was followed. First, a stock solution of 12.5 mL of 0.1% graphene oxide was prepared using MiliQ-water®. Then, the same reduction treatment with $NaBH_4$ by reflux was followed in the three procedures, the washing and drying processes were changed.
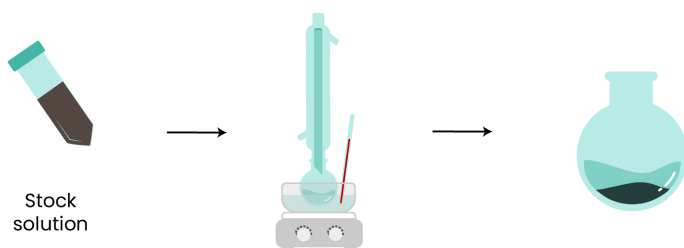
Figure 3.5: First procedure for reduction of graphene oxide.

First Procedure Using 3.12 mL from the stock solution, 0.289 g of $NaBH_4$ was measured to react with the aqueous GO in a reflux condensation process with constant magnetic stirring for 24 h at 80 °C. The heating method was performed with a mineral oil bath, instead of water, to prevent its evaporation. The resulting graphene solution was washed with DW and it was oven-dried under vacuum at 65 °C. Graphical representation of this process is shown in Figure 3.5.
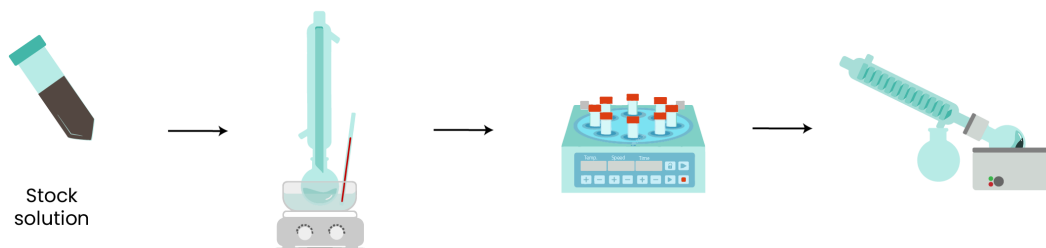
Figure 3.6: Second procedure for reduction of graphene oxide.

Second Procedure The same chemical reduction as the first procedure was performed. However, the resulting graphene solution was centrifuged for 10 minutes at 2500 rpm and was washed with DW. This process was performed at least 3 times to clean up any residue of $NaBH_4$ that did not get to react. The substrate was placed into a rounded-bottom flask to get dried in the rotovapor at 62 °C for 3 h, the result can be observed in Figure 3.7. Filtration processes were avoided in order to retain as much substrate as possible. This separation and drying of the substrate were done to obtain a material with fewer impurities. A graphical representation of this process is shown in Figure 3.6.

Figure 3.7: rGO obtained after the second methodology for chemical reduction of GO with $NaBH_4$
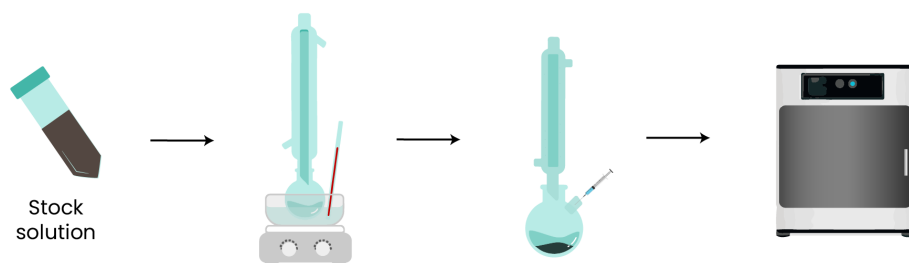
Figure 3.8: Third procedure for reduction of graphene oxide.

Third Procedure The same chemical reduction as the first and second procedure was performed. Different samples were taken with a syringe for different reduction times: 3h, 6h, 17h, 18h, 21h, 27h, and 42h. However, in this case, the resulting aqueous material was dried on a stove at 70 °C for 4 hours. A graphical representation of this process is shown in Figure 3.8.

Finally, in Figure 3.9 rGO samples of different reduction times can be observed in a) aqueous solution after the third reduction treatment and before drying for 4 hours in the oven. In b) side samples were placed on slides and later taken for characterization in Raman.
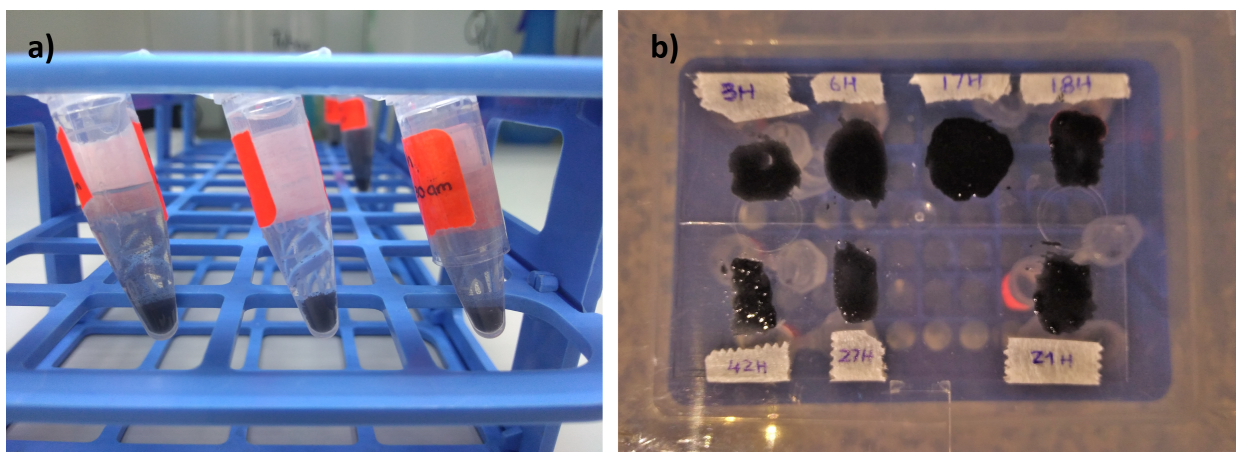
Figure 3.9: rGO samples a) in aqueous solution before being dried, and b) before being characterized at Raman spectrometer.

3.2.4 rGO Deposition on OF

Fibers were immersed in a 0.5% rGO solution in intervals of 30 s, and 30 s of delay between each dive. OF with rGO deposited (OF-rGO)s were let dried in room temperature. Then, OF-rGOs were annealed by placing them in a furnace heated to 700 °C with a heat rate of 50 °C/h during 26 h and the last temperature (700 °C) was held for 1 h. A constant inlet Ar_2 flow of 2 L/min (14 ml/h) was remained throughout. The furnace was left to cool down to room temperature for 2 hours.
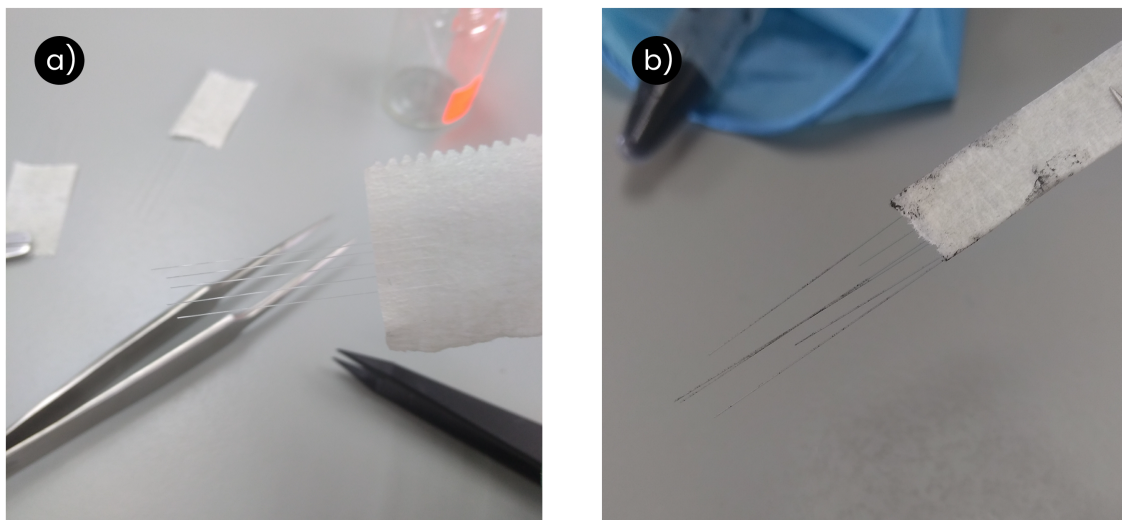
Figure 3.10: Fibers with rGO attached after annealing process a) before, and b) after.

3.3 Characterization

3.3.1 Raman Spectroscopy Characterization

Raman characterization for rGO was carried out in ambient conditions by using LabRAM HR Evolution Raman Spectrometer HORIBA, Figure 3.11, belonging to Yachay Tech University, Ecuador, spectrometer. Since samples did not present fluorescent emission 532 nm was chosen

as the laser excitation wavelength with a 100× objective at room temperature. The spectrometer was calibrated in frequency with the Rayleigh peak to be set at 0 cm^{-1}.

Figure 3.11: LabRAM Raman Spectrometer HORIBA, Yachay Tech University, Ecuador.

3.3.2   Fitting and Graphic Methodology

Three software were used for the fitting procedure: Peak-O-Mat, PeakFit, and Origin Pro.

Peak-O-Mat version 1.2.9 is a Python-based program that allows cleaning, transforming, fitting, calibrating, etc., of raw spectroscopic data. The software was used for setting operations to normalize the G-band intensity. PeakFit version 4.12 is an automated analysis software that allows to locate of the characteristic peaks of the spectroscopy data and find the best equation that fits the data through a non-linear separation. Being a non-linear curve fitting, it allows an accurate analysis of the peaks, as it reduces noise while maintaining the integrity of the original data. It was used to deconvolve several peaks including electron-poor carbon, electron-rich carbon, sp2 C-C, C-O, C=O, and O-C=O with Gaussian, Voigtian, and Lorentzian functions. The amplitude parameters of the Voigtian function, center of the function, FWHM Lorentzian, and FWHM Gaussian, in a region from 1100 to 1800 cm^{-1} were examined. Origin Pro 2018 is not only a tool for data analysis but it is also a graphing software. Origin offers a worksheet that allowed manipulation the data by associating attributes like peak intensity with operation formulas.

3.3.3 Optical Microscope Characterization

For the analysis of the state of the optical fiber before surface treatment, the Leica model DM300 binocular microscope was used.

3.3.4 SEM Characterization

SEM micrographs were taken with X-Ray Photoelectron Spectroscopy (XPS) PHI VersaProbe III (Physical-Electronics) equipped with SEM Microprobe provides scanning X-ray induced secondary electron images (SXI) generated by scanning a focused sub-10 m X-ray beam across the sample. In this way, the SEM used is not an isolated equipment but an additional instrument inside the XPS; only secondary electrons were the carriers for topographic information but not backscattered electrons. Samples were prepared in a carbon substrate and the characterization was performed under high vacuum.

Chapter 4

Results & Discussion

The results from the optical microscope show the OF coatings used by communication companies for allowing its operation as an information transmitter, which has 100 μm of diameter and 6e+4 μm of length. In micrographs of Figure 4.1, it can be observed several transparent fibers with a nibbled appearance in a) at 25x. External manipulation of OF exposes the polymeric covering as it is easily cracked. In images b) and c), 100x and 160x, respectively, it can be noticed a double layer in the fiber. As explained in the methodology, OF underwent a muffle treatment, in which a temperature below the melting point of SiO was used to calcine the mentioned coatings, and subsequently, piranha solution was used to remove any other adhered debris. By following this
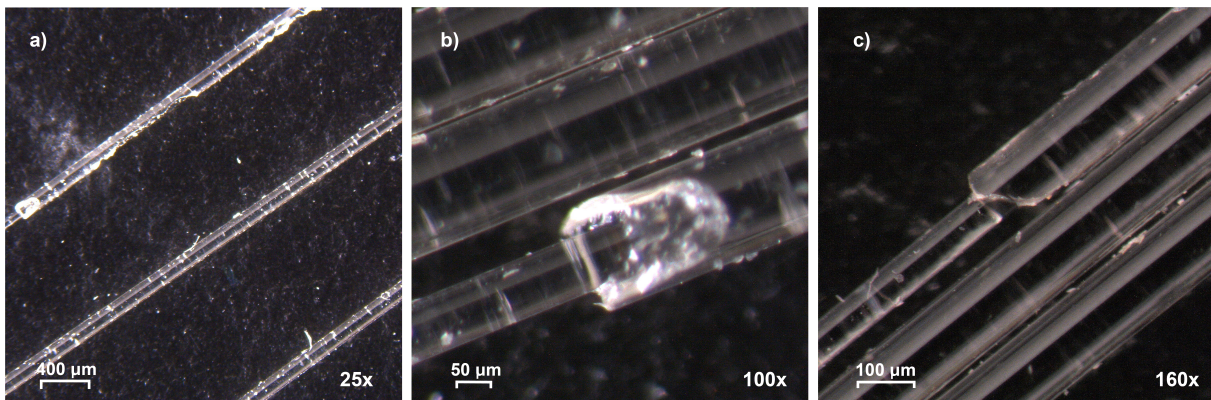
Figure 4.1: Optical microscope OF micrographs showing polymeric coating before piranha solution treatment.

treatment, OF remained free from cracking and chipping, in comparison with Figure 4.1. OF were washed with ethanol and stored in N_2. On the other hand, in graphene micrographs from Raman spectroscopy, features like peak positions, FWHM, amplitudes, and intensity ratios are analyzed from the band peaks D (1350 cm^{-1}) and G (1580 cm^{-1}), which are the principal indicators of carbon materials. This last is the fingerprint of both graphite and graphene structures; then, the D band is the one that establishes a difference since is very sensitive to irregularities in graphite structures since resonance in the D band is directly proportional to the vibrational process. In this way scattered electrons activate the disorder in the crystal symmetry; and so too, it is related to the amount of crystallite in the boundaries and interfaces too. Figure 4.2 shows Raman spectra obtained after GO reduction during different periods (3, 6, 17, 18, 21, 27, and 42 h). As mentioned
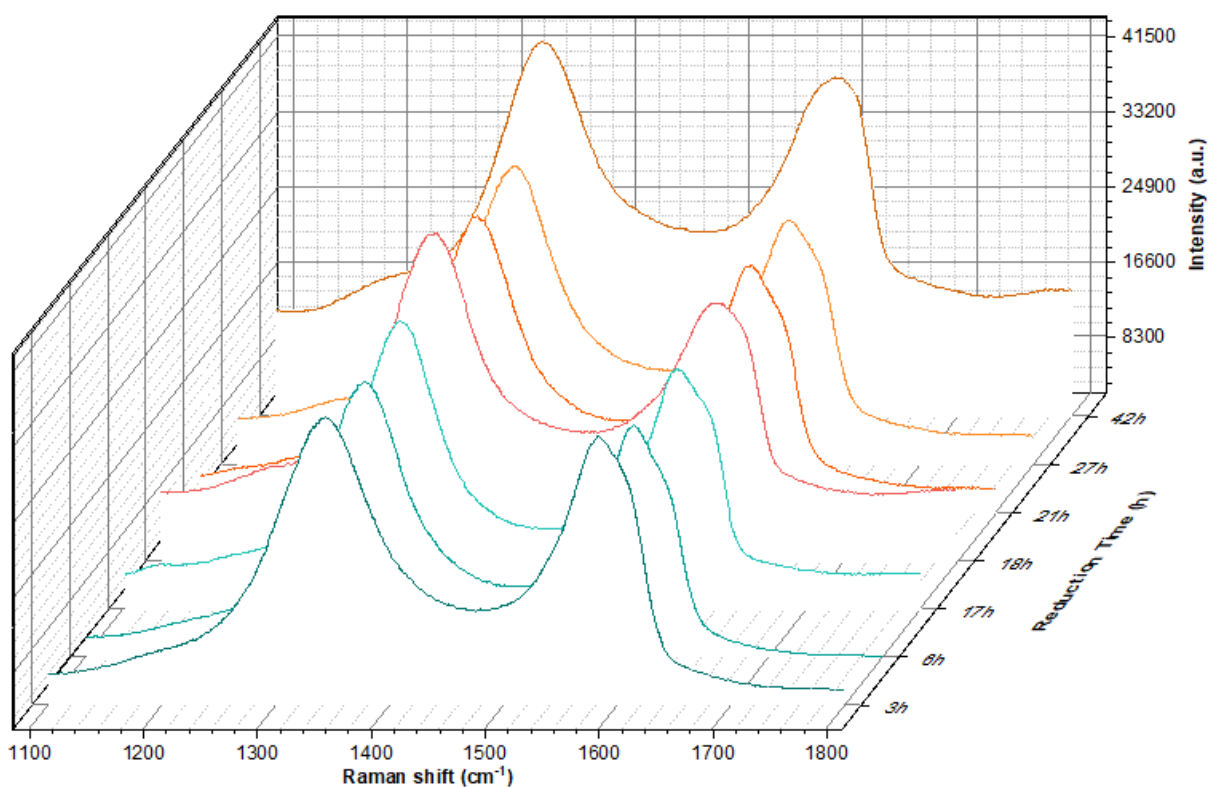
Figure 4.2: The waterfall plot of Raman spectra of rGO reduced with NaBH$_4$ from 3h to 42h. The D and G bands are observed respectively.

above, a fitting process was carried out with PeakOMat and Peakfit software and the range from 1100 to 1800 cm^{-1} was determined for the analysis. At first glance, it can be seen that all reduction cases show disorder in the graphitic material. Particularly, an obvious growth in intensity and FWHM is observed at D and G bands for the maximum case of rGO, 42 h. Furthermore, it can be seen that some of the curves are not symmetric especially for the G band. Also, as presented in Figure 4.3, Raman spectra presents the D band has a higher intensity than G band, which is normally expected for an rGO material to which different impurities have been introduced, such as functional groups that alter the symmetry of the honeycomb. Precisely due to the D band results from a phonon lattice vibrational process and exhibits a dispersive behavior in the presence of defects or disorders in the sp^2 hybridized carbon layer. In other words, the D band indicates the number of defects in the rGO. The D band, in all the reduction cases, are shifted out from its particular signal value, and this band experiences a greater shift than the G band while increasing the reduction time. Instead, the G band describes a movement towards higher frequencies, which, as mentioned in the theoretical background section, a positive shift for the G band is related to compressive strain. For a correct Raman analysis of rGO, one cannot simply take the intensities shown in the graphs. In Figure 4.4 side a), the initial result of the case of reduction of graphene and its three main bands D, G, and 2D is observed; however, during the analysis and fitting of the Raman peaks of rGO, there were small shoulders that are normally ignored. Some authors fit these shoulders through 5 to 8 deconvolution bands, respectively in the experimental works carried out by Claramunt et al.[48] and Vecera et al.[49]. Unlike Vecera's work where all eight functions that were used for fitting were Voigtian, Claramunt's work reports the use of three pseudo-Voigtian and two Gaussian functions. In this analysis six Voigtian functions were used for fitting, D and G occupy the aforementioned position 1350 and 1580 cm^{-1}, respectively. Peaks D*, D''', D'', and D' are added for the positions 1180, 1450, 1550, and 1610 cm^{-1}, respectively. Figure 4.5 shows an example of the deconvolution performed. In red straight line, it is shown the fitting data, and in black open circles the experimental data. Each one of these Raman bands are relates with specific bonds. G belongs to the sp^2 energy of C-C bonding type and by its shifting and FWHM indicates the conservation of the graphene layers. D band is related to the C_A-C_B bonding type. The D* band, located at the beginning of the spectrum, is related to the graphitic disorder of the lattice by sp^2-sp^3 bonds at the edges.[48] Further information can be corroborated in the annexes section where the graphs of deconvolution and assignments of the Raman modes of rGO are described
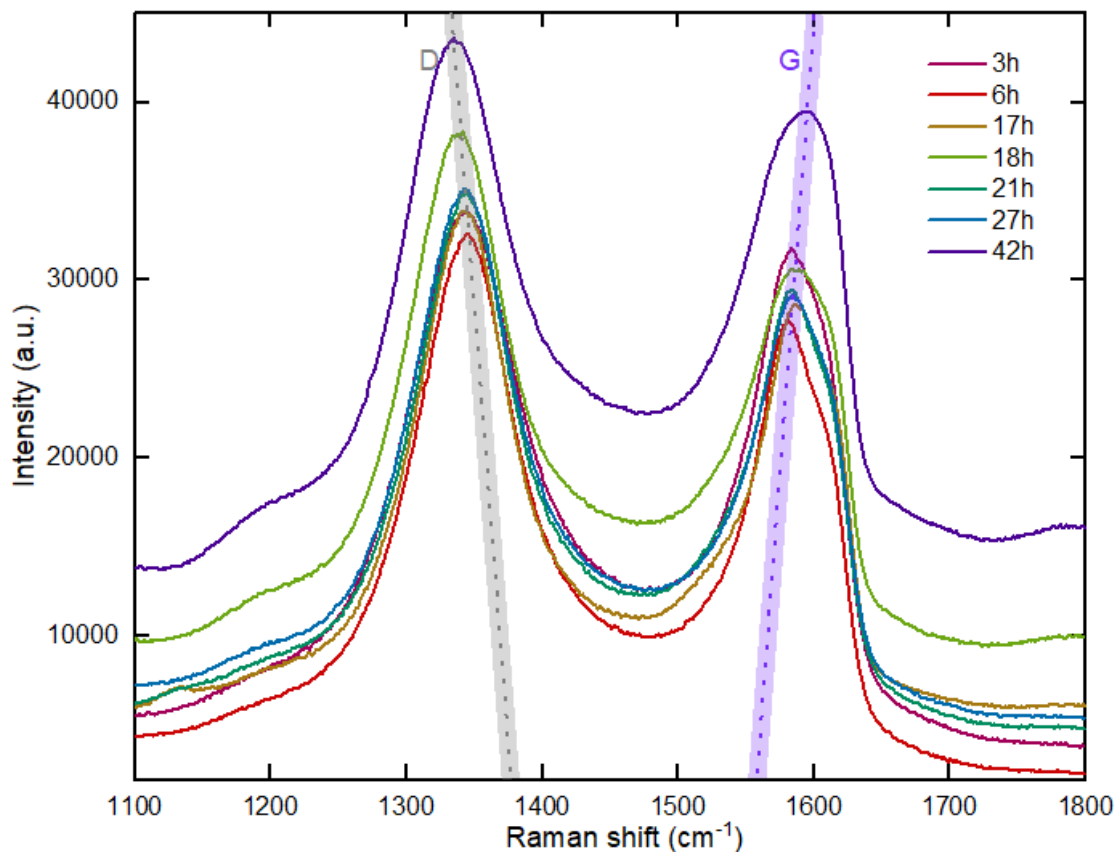
Figure 4.3: Raman spectra for D (gray dotted highlight) and G (purple dotted highlight) bands. Raman spectroscopy of graphene exposed in different reduction times. Laser excitation used: 532 nm.

for all reduction times. Band D''' is related to C_B-C_C bonding type.[49] Band D'' is associated with interstitial defects of amorphous sp^2 bonds that can include functional groups.[48] Finally, the D' band describes disordered-induced phonon mode provoked by the crystal defects[48], also related to C_C-C_D bonds.[49] Figure 4.6 shows in greater detail the change in intensities of the D band, as it increases the number of defects also does. It can be seen that there is a shifting to lower frequencies, shown in the dotted blue line, beginning in 1343 cm^{-1} for 3h reduction case and ending at 1335.09 cm^{-1} for 42h reduction case. This shifting is caused by a breakdown of the C_A-C_B structure. Shifting also can occur because to the D band underlying modes are sensitive
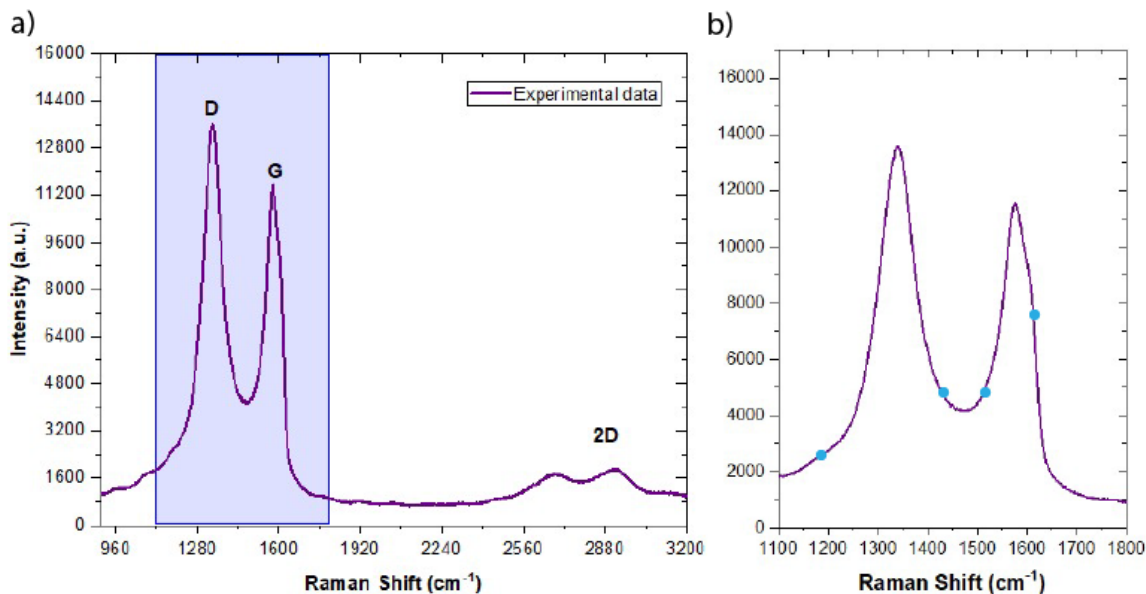
Figure 4.4: Raman spectra of a) bands D, G, and 2D obtained from the experimental data of rGO. By taking a closer look at the D and G bands, in b) (magnification of the blue region in a)), four shoulders (doted) are found on both bands of rGO. The example spectra is taken from 3h reduction case.

to the excitation laser used, although 532 nm was used for all measurements. FWHM in the D band is noted to get broader as the reduction time increases which indicates more defects. On the other hand, the G band intensity variation, which is shown in Figure 4.7, contrary to the D band it presents a shift at higher frequencies, shown in blue dotted line, beginning at 1583.16 cm^{-1} in a reduction of 3h where the initial graphitic material has a modified lattice structure due to oxidation and ends in a 42 h reduction which band moves to higher frequencies (1596.41 cm^{-1}) for a less oxidized material and partially recovering of sp^2 hybridization due to the more time for reduction. While the G band is normally assigned in the range of 1550 to 1575 cm^{-1}. The intensity increase from a material reduced by 3h to one with a maximum reduction of 42h, is ~25%. Another special detail is the presence of a shoulder on the right side of the G band in the samples, which increases the FWHM of the peaks, as it is clear in the 18h case. However,
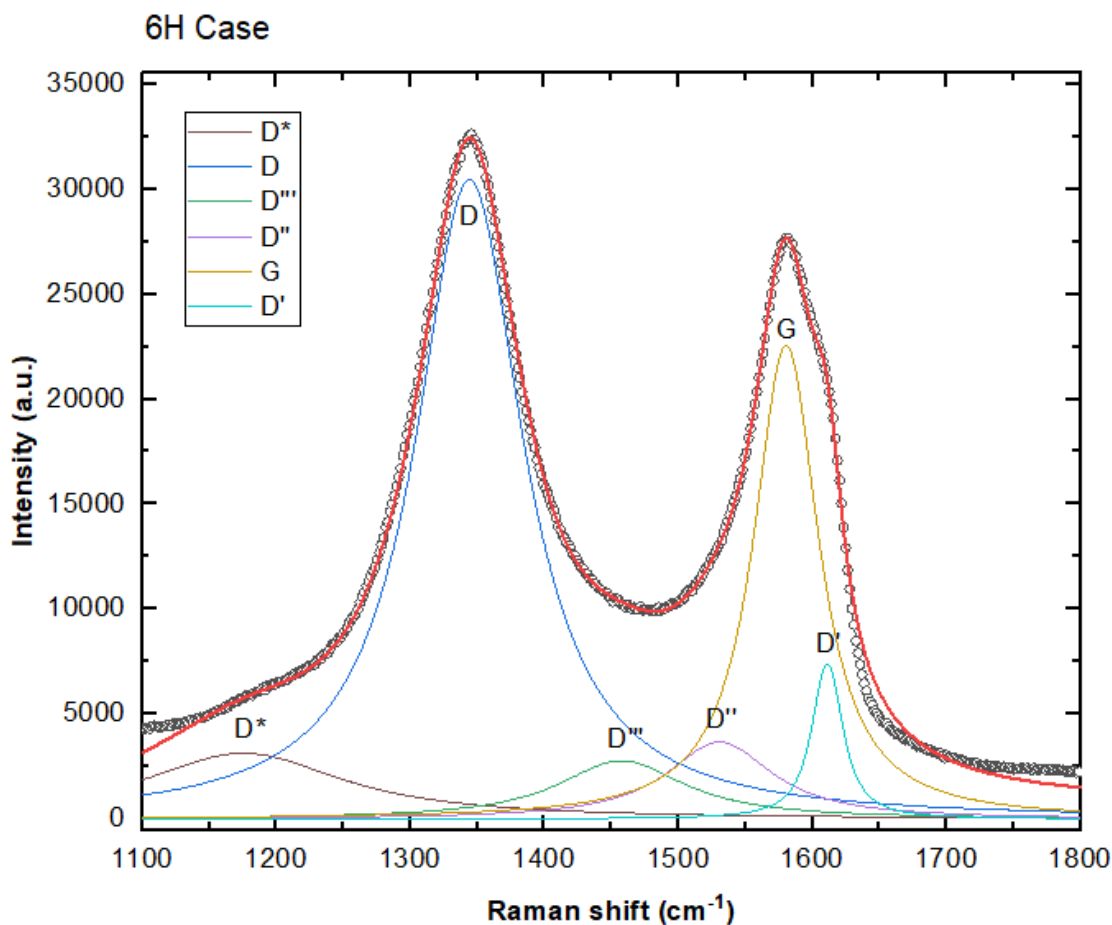
Figure 4.5: Six Voigtian functions (D*, D, D', D", D"' and G Raman bands) deconvolution for the rGO obtained. Fit data in red line and experimental data in open black circles

note that in the reduction time of 42h the shoulder does not exist while FWHM increases. This shoulder appearance occurs since the G band is deconvoluted in three Raman bands. The 21h and 27h cases do not present a significant difference in intensities and shifts. Also, note that the highest intensities are found for the first and last case of reduction. The intensity ratio between the D band and G band is also calculated in order to determine the number of defects in the structures. Figure 4.8 shows that this ratio, based on the reduction times, is above 1.00 in all the measurements. This implies high defective lattice for all rGO reduced samples. The 6h and 17h reduction cases present the lowest ratio values, while in 18h of reduction rGO gains defects
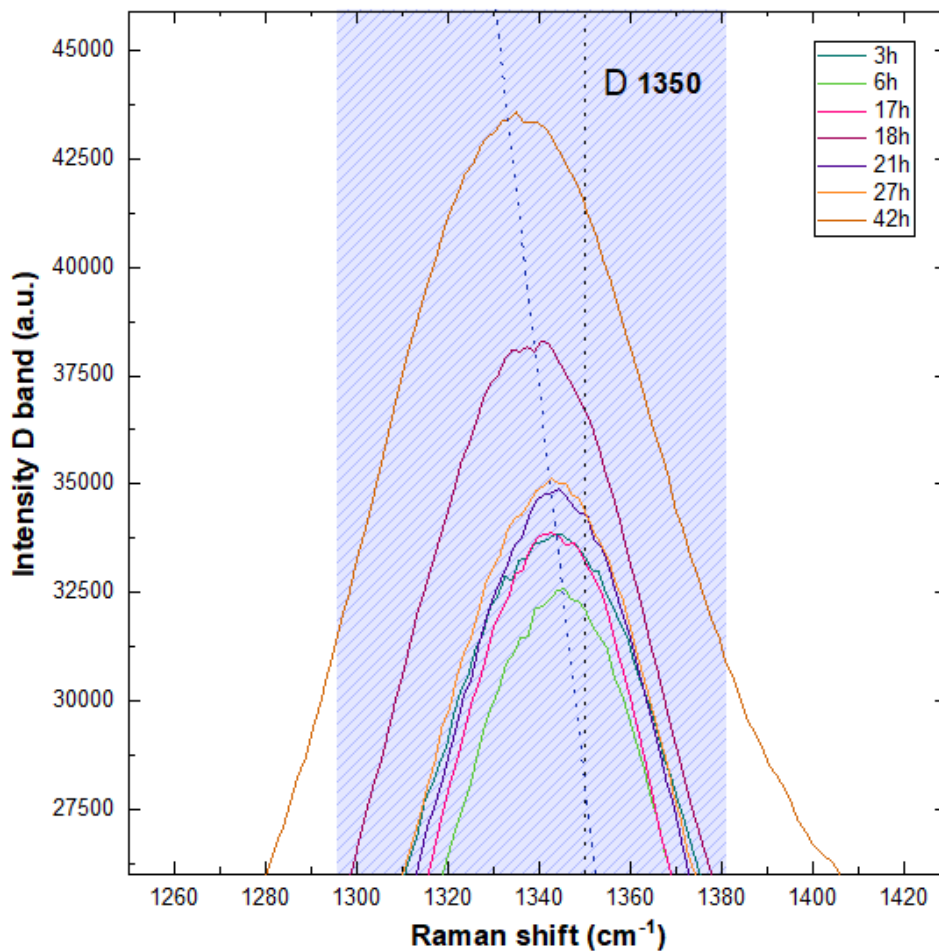
Figure 4.6: Raman spectra of the rGO D band intensity. Black dotted line shows the characteristic position of the D band at 1350 cm^{-1}, blue dotted line shows the position shifting towards lower energies obtained from the reduction experimental data.

again. Also, it is important to highlight reduction by 42h in which the radius I_D/I_G is significantly increased, suggests a higher amount of oxygen defects breaking the symmetry. The difference of defects between the initial and final material according to the I_D/I_G ratio is about 42%. Although initially it could be interpreted that the cases 21h and 27h are very similar, Figure 4.8 shows the opposite when taking into account FWHM by showing that the case of 27h has a greater number
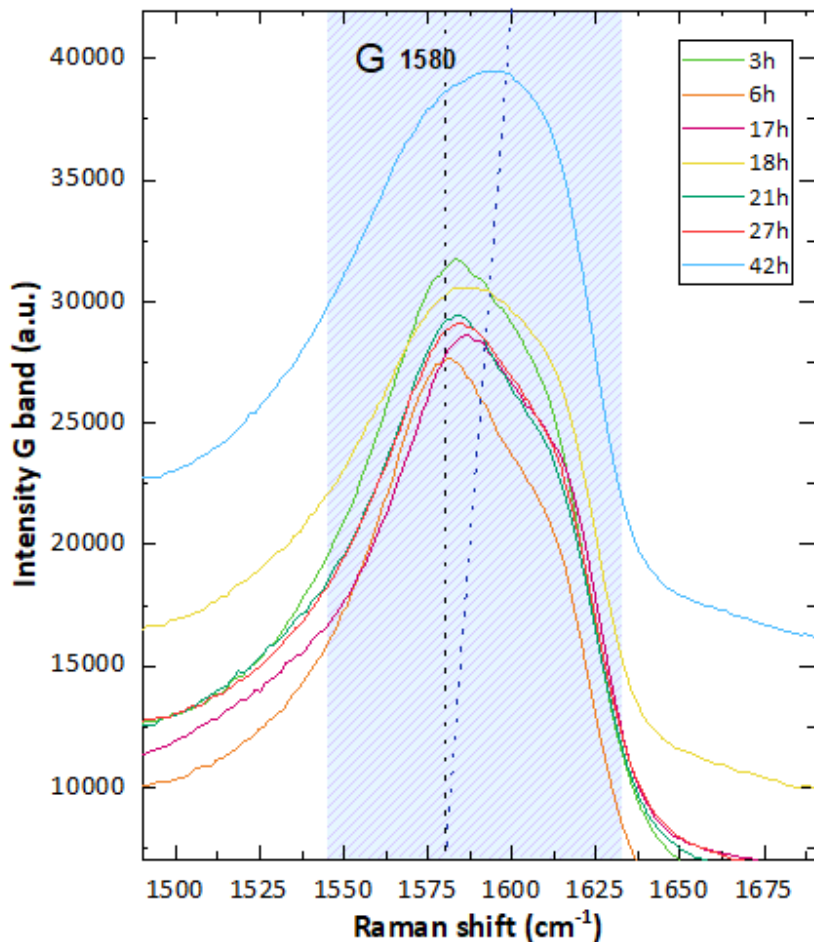
Figure 4.7: Raman spectra of the rGO G band intensity. Black dotted line shows the characteristic position of the G band at 1580 cm^{-1}. Blue dotted line shows the position shifting towards higher energies obtained from the reduction experimental data.

of defects. The 6h case is the one with the lowest intensity in the D band (less disorder), but also the one with the least intensity in the G band indicating a reduction in the number of layers. The 18h reduction case, as mentioned before, shows quite a defective material, which is what its D band indicates, although it is a short period reduction in comparison with the 42h case. The D* band was also analyzed, which as mentioned is associated with sp^2 and sp^3 defects, the
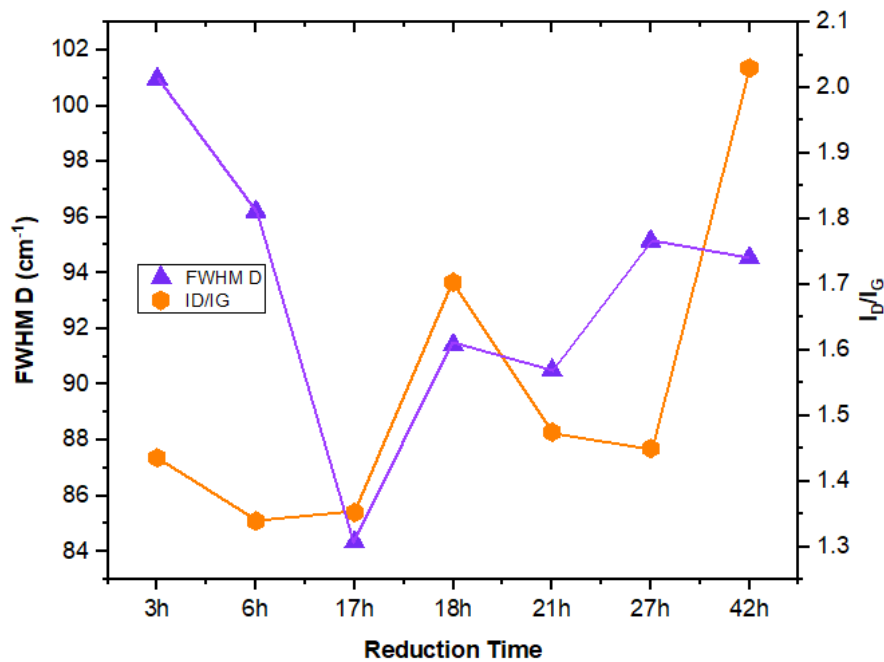
Figure 4.8: Evolution of ratio I_D/I_G bands (yellow hexagons), and FWHM of the D band (purple triangles) for different reduction times.

I_{D*}/I_G ratio is shown in Figure 4.9. At a glance, an appropriate pattern was not found that allowed identifying a dependence on defects in the rGO material with the reduction time. However, it can be identified that there is a growing trend from the case of reduction at 6h to 27h cases present the highest I_{D*}/I_G ratios, while 3h and 17h (initial reduction periods) have the lowest I_{D*}/I_G ratios. On the other hand, at FWHM of D* it is found that cases of 6h and 21h have the highest FWHM. Both cases 6h and 27h, are the ones that register the highest FWHM while the highest I_{D*}/I_G implies a high content of defects in sp^2 and sp^3 bonding at the edges.

In the analysis of the D''' band, represented in Figure 4.10, which is associated with the sp^2 interstitial defects of the graphene crystal, it is found that the FWHM is high (206.72) for the initial reduction case, decreases to 87.6 in the reduction by 17h and returns to increase to 146.05 in the final reduction time. This indicates that the reduction of 17h inte the rGO material presents
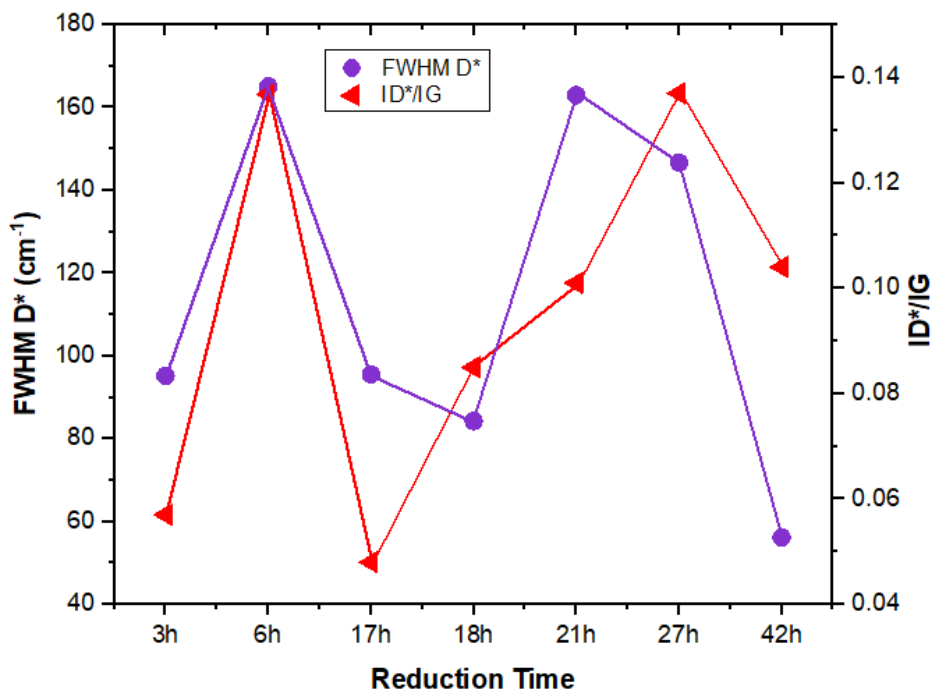
Figure 4.9: Evolution of ratio I_{D*}/I_G bands (red triangles) and FWHM of the D* band (purple circles) for different reduction times.

fewer defects and greater crystallinity. This can be concluded based on the study carried out by Claramunt et al.[48]. The ratio of the intensity of the Raman band D''' and G band exposes that the case of 17h rGO reduction is found to be the lowest. While in the last reduction case $I_{D'''}/I_G$ ratio is the highest. Besides, under the interpretation of Claramunt[48], the oxygen concentration can be estimated by using the position of the bands. Figure 4.11 shows a comparison of the displacement of the peaks D*, G, and D''' is observed. D* band (squares) shifts to their minimum positions in the 6h (1175.5 cm^{-1}) and 21h (1176.5 cm^{-1}) reductions. G band (circles) presents a mild shifting, beginning from 1581 cm^{-1} at 3h case to 1577.5 cm^{-1} at 42h case. By taking into account the position of the D* band and the work carried out by this author, it can be suggested that the oxygen content in the sample prevails in the range of 15 to 25%. In his work it is described that the cases with red shift present a greater amount of oxygen, associating this interpretation it can be suggested that the cases of 6h and 21h are those in which there is a higher oxygen content. It is
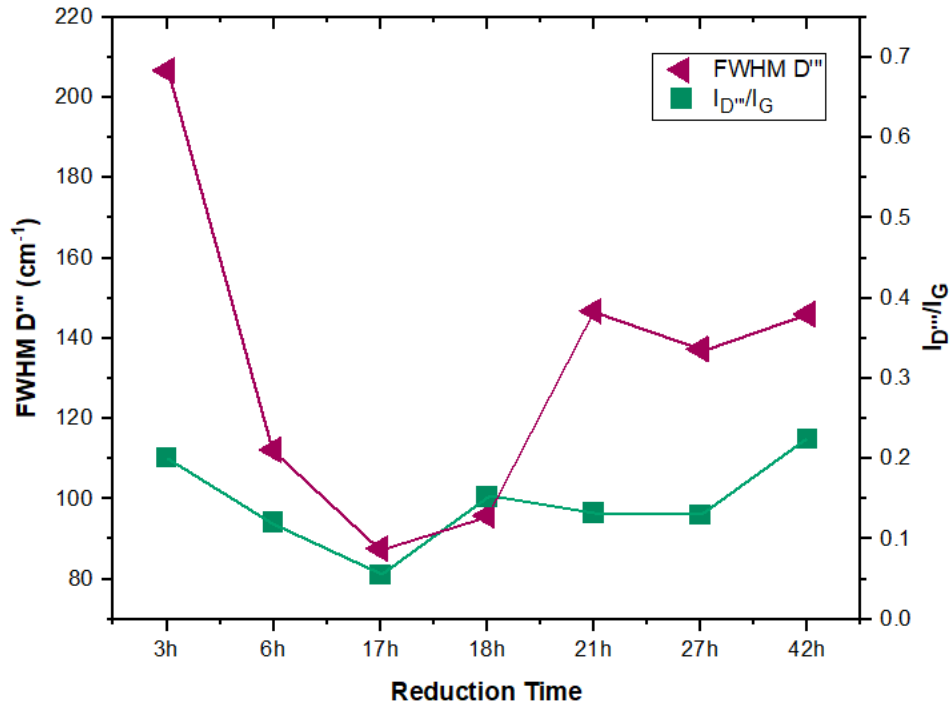
Figure 4.10: Evolution of ratio $I_{D'''}/I_G$ (green squares) bands and FWHM of the D''' band (purple triangles) for different reduction times.

also necessary to take into account, as mentioned above, that this band is related to the interstitial defects provided by sp^2 bonds at C_B-C_C. In Figure 4.12, it can be seen that the Raman bands with the highest intensity are those of D' and D'' for the case of 42h reduction and the D' band for the case of 3h. By making an average of the values we can indicate that the case of reduction that contains less intensity in the contribution of these bands are the cases 17h, 18h, and 21h.
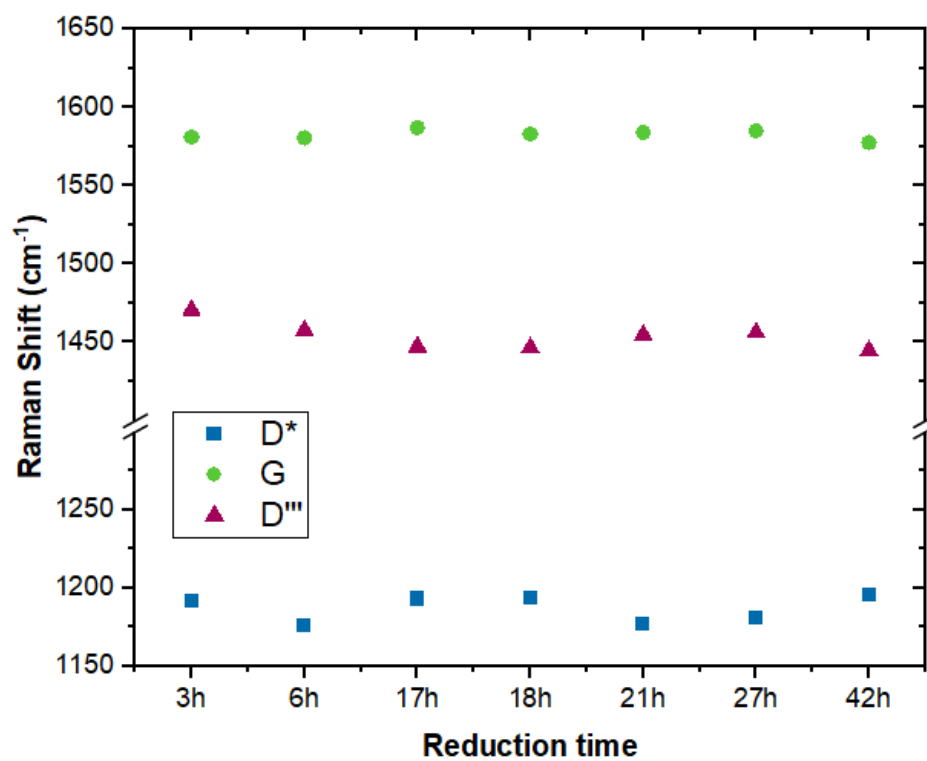
Figure 4.11: Position shifting variation of G band (circles), D* band (squares), and D'" band (triangles)
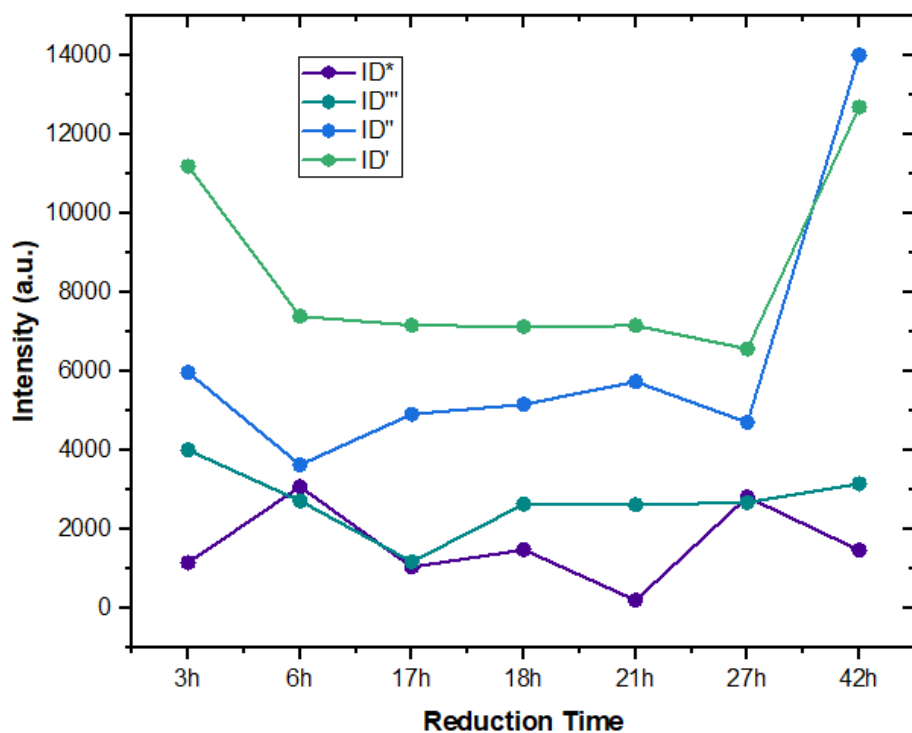
Figure 4.12: Intensity comparison of bands D*, D', D" and D"' according to the different reduction times.

Chapter 5

Conclusions & Outlook

For the production of miniaturized electrochemical sensors, it is important to develop a proper connection between nano/micro scales and an efficient material for sensing purposes. So, in this work, we focus on the study of a novel design of high-performance miniaturized electrodes based on rGO for surface-modified silica fiber. In this way, the experimental methodology are divided into two main procedures: on the one hand, graphene oxide material was reduced to rGO by a chemical oxygen reduction method with the reducing agent, $NaBH_4$. On the other hand, the surface OF electrodes was cleaned and modified with 3-aminopropyltriethoxysilane (APTES), and depositing with the resulting rGO material. The characterization of the modified rGO and the modified surface were carried out using Raman spectroscopy and SEM, correspondingly.

The chemical oxygen reduction method was performed to recover the electrical properties of graphene. The reducing agent, $NaBH_4$, was chosen due to it allows a simpler and more affordable synthesis of rGO, and have previously reported more effective results than other reducing agents. The procedure consist in perform a reflux reduction treatment of 3.12 mL of aqueous GO with 0.289 g of $NaBH_4$. Three types of drying were carried out for the final resulting samples, as mentioned in the Methodology section, and only the third procedure was studied. From this, different rGO samples were taken at 3h, 6h, 17h, 18h, 21h, 27h, and 42h. Those aqueous solutions were dried in a oven previous Raman characterization.

The Raman spectroscopy was used for the characterization of the seven resulting rGO samples, the spectra show us that the exposure time to $NaBH_4$ is leading for getting the different levels of reductions, and so defects, in the rGO material. Raman spectra of rGO of the different reduced

times were analyzed and the results showed that the best reduction time, taking into account the quality of the material, was observed for 6h reduction case. To this must be added that a proportional amount of $NaBH_4$ used is a delimiting factor in the process. In this way, it would be expected that by providing a greater amount of this inorganic compound, the graphitic material would expose fewer defects and in less reduction time. Six Raman bands were reported (D*, D''', D'', D', D and G) that relate the experimental works of Vecera et al.[49] and Claramunt et al.[48] who worked with seven and five Raman bands, respectively. It was noted that the longer the reduction time the amount of defects represented by the D band increased. By analyzing I_D/I_G ratio it was found that the longer the reduction time the graphitic character of the material decreased represented by G band, while D band presented a shifting to 1335 cm^{-1} in that case.

Also, $I_{D'''}/I_G$ ratio showed its relationship with sp^2 and FWHM of D''' decreased for 17h of reduction. When increasing the reduction time the intensity ratio increases suggesting the increment in interstitial defects in graphene oxide. The method of chemical reduction of graphene with sodium borohydride demonstrated to be an effective and convenient procedure for getting significant quality GO with non-permanent defects that can be remove for best results when increasing the time of reduction for a certain molar concentration of this reducing agent.

For OF a SEM characterization was performed to estimate the external polymeric coating. The cleaning of the surface OF electrodes was performed by a muffle furnace in oxidizing atmosphere at 700 °C for 2h and then piranha solution for organic residues removal and for introduction of hydroxilate groups. OF surfaces were modified with 3-aminopropyltriethoxysilane (APTES) in a reflux treatment. Later, a SEM characterization was not carried out. OF were immersed in a 0.5% rGO solution, then OF-rGO were annealed for a successful deposition of rGO.

In conclusion, 6h GO reduction case shows the best rGO quality in relationship with the concentration of $NaBH_4$ used, which interbands in Raman spectra demonstrate fewer variation in its graphitic structure. Oxygen concentration was compared with Claramunt's[48] work and shows to have a range of 15 to 25% of oxygen-containing groups. APTES treatment for OF carried out showed a proper method for deposition of rGO in the material.

Further investigation is still open specifically for variation in the reducing agent $NaBH_4$ concentration and for analysis in the different Raman interbands and its relationship with crystallinity and introduction of functionalities. From this, a Raman characterization is proposed for OF-rGO immersed in 0.5% rGO solution to appreciate the graphene distribution on the silica surface.

Likewise, it is important to experiment with the assembly of electrodes immersed in higher concentration rGO solutions. In this transferring process of the graphene layers to the silica-based electrodes, an important subsequent challenge would avoiding rolling, wrinkling, cracking and tearing of rGO. Finally, an electrochemical analysis must be carried out to identify the electrical capacity of the electrodes. This suggest its possible application for detection of contaminants; its portable size would also allow the electrodes to monitor not only in water treatment plants but also at pipelines and points of supply and use.

Appendix

This section presents the results of Raman characterization of the GO reduction with NaBH$_4$ for 3h, 6h, 17h, 18h, 21h, 27h and 42h in that order. These results show the experimental data, fitting data and the fit of the 6 Voigtian functions used for the deconvolution of the main bands D and G. Likewise, tables have been added that show the features to which each band corresponds. These bands G, D, D '' 'and D' have a peak assignment of towards the links CC, C$_A$-C$_B$, C$_B$-C$_C$ and C$_C$-C$_D$, while the bands D *, D '' have an unknown assignment until the date.
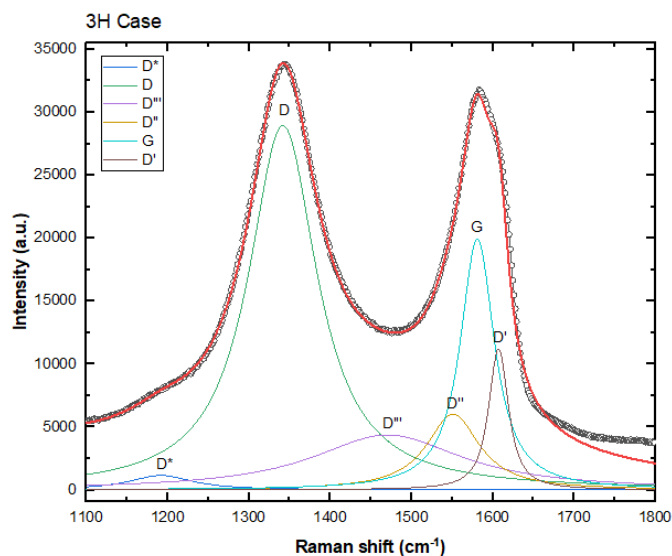
Figure 5.1: Raman bands deconvolution for 3H rGO

Table 5.1: Raman spectra deconvolution for 3H rGO

Peak Assignment	Raman mode	FWHM	Intensity	Fitting position [cm^{-1}]	Reference position [cm^{-1}]
C-C	G	50.53	19924.25	1581	Claramunt[48], Vecera[49]
C_A-C_B	D	100.97	28604.73	1341.5	Claramunt[48], Vecera[49]
	D*	95.21	1144.94	1191.5	Vecera[49]
C_B-C_C	D'''	206.72	4003.61	1470.5	Claramunt[48], Vecera[49]
	D''	78.61	5974.32	1551	Vecera[49]
C_C-C_D	D'	29.25	11196.17	1607	Claramunt[48], Vecera[49]
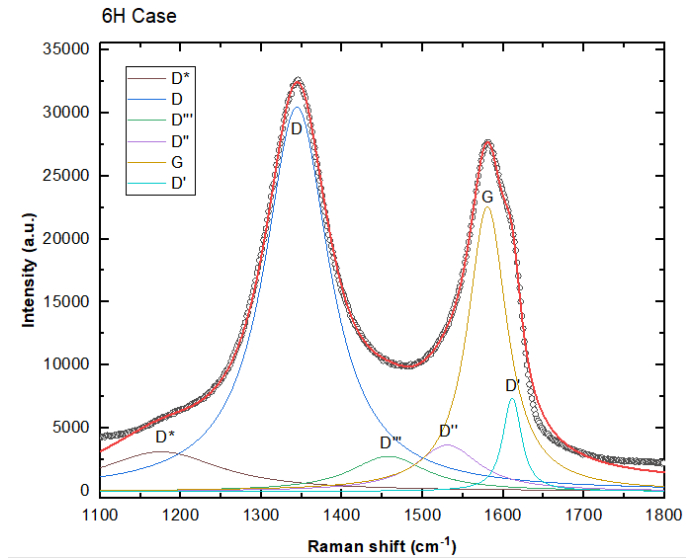
Figure 5.2: Raman bands deconvolution for 6H rGO.
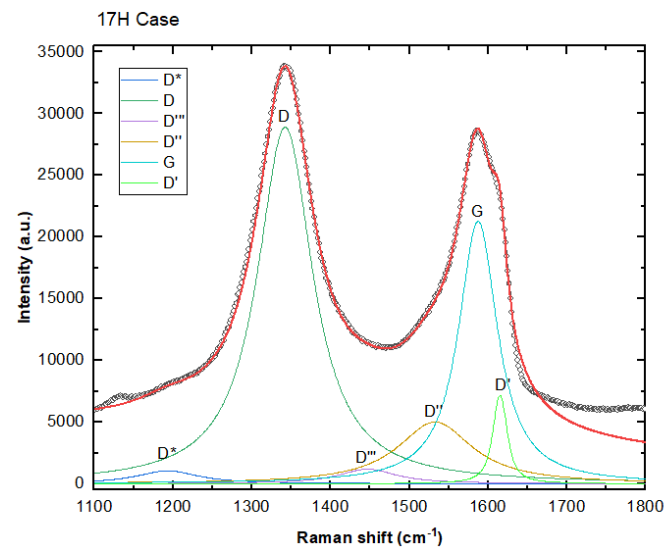
Figure 5.3: Raman bands deconvolution for 17H rGO.

Table 5.2: Raman spectra deconvolution for 6H rGO

Peak Assignment	Raman mode	FWHM	Intensity	Fitting position [cm^{-1}]	Reference position [cm^{-1}]
C-C	G	58.60	22468.53	1580.5	Claramunt[48], Vecera[49]
C$_A$-C$_B$	D	96.21	30087.43	1344	Claramunt[48], Vecera[49]
	D*	165.06	3073.46	1175.5	Vecera[49]
C$_B$-C$_C$	D'''	112.22	2714.38	1457.5	Claramunt[48], Vecera[49]
	D''	95.26	3624.89	1531	Vecera[49]
C$_C$-C$_D$	D'	27.77	7394.19	1611	Claramunt[48], Vecera[49]

Table 5.3: Raman spectra deconvolution for 17H rGO

Peak Assignment	Raman mode	FWHM	Intensity	Fitting position [cm^{-1}]	Reference position [cm^{-1}]
C-C	G	59.45	21191.56	1587	Claramunt[48], Vecera[49]
C$_A$-C$_B$	D	84.34	28653.58	1342.5	Claramunt[48], Vecera[49]
	D*	95.58	1037.89	1193	Vecera[49]
C$_B$-C$_C$	D'''	87.60	1166.71	1447	Claramunt[48], Vecera[49]
	D''	113.46	4913.49	1532.5	Vecera[49]
C$_C$-C$_D$	D'	21.66	7165.81	1615	Claramunt[48], Vecera[49]
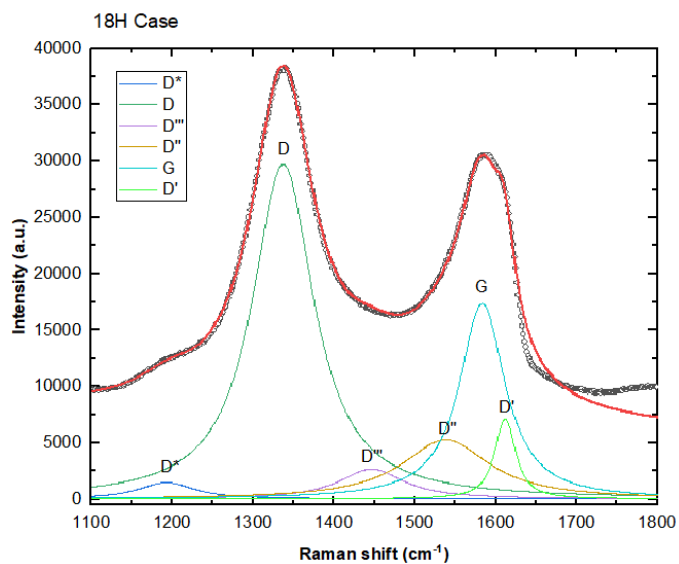
Figure 5.4: Raman bands deconvolution for 18H rGO.
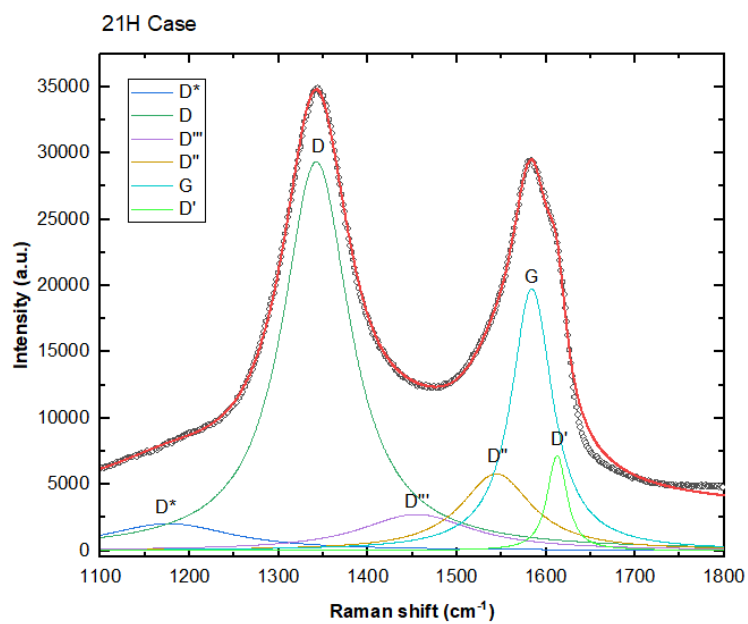
Figure 5.5: Raman bands deconvolution for 21H rGO

Table 5.4: Raman spectra deconvolution for 18H rGO

Peak Assignment	Raman mode	FWHM	Intensity	Fitting position [cm^{-1}]	Reference position [cm^{-1}]
C-C (graphene)	G	67.73	17300.31	1583	Claramunt[48], Vecera[49]
C$_A$-C$_B$	D	91.42	29466.94	1337.5	Claramunt[48], Vecera[49]
	D*	84.26	1478.183	1193.5	Vecera[49]
C$_B$-C$_C$	D'''	95.85	2632.76	1446.5	Claramunt[48], Vecera[49]
	D''	128.89	5163.91041	1538	Vecera[49]
C$_C$-C$_D$	D'	31.06	7130.28	1611.5	Claramunt[48], Vecera[49]

Table 5.5: Raman spectra deconvolution for 21H rGO.

Peak Assignment	Raman mode	FWHM	Intensity	Fitting position $[\text{cm}^{-1}]$	Reference position $[\text{cm}^{-1}]$
C-C (graphene)	G	55.45	19710.71	1584	Claramunt[48], Vecera[49]
C_A-C_B	D	90.51	29071.01	1342	Claramunt[48], Vecera[49]
	D*	163.00	1997.41	1176.5	Vecera[49]
C_B-C_C	D'''	146.81	2617.10	1454.5	Claramunt[48], Vecera[49]
	D''	95.64	5734.94	1544	Vecera[49]
C_C-C_D	D'	26.49	7158.30	1612.5	Claramunt[48], Vecera[49]
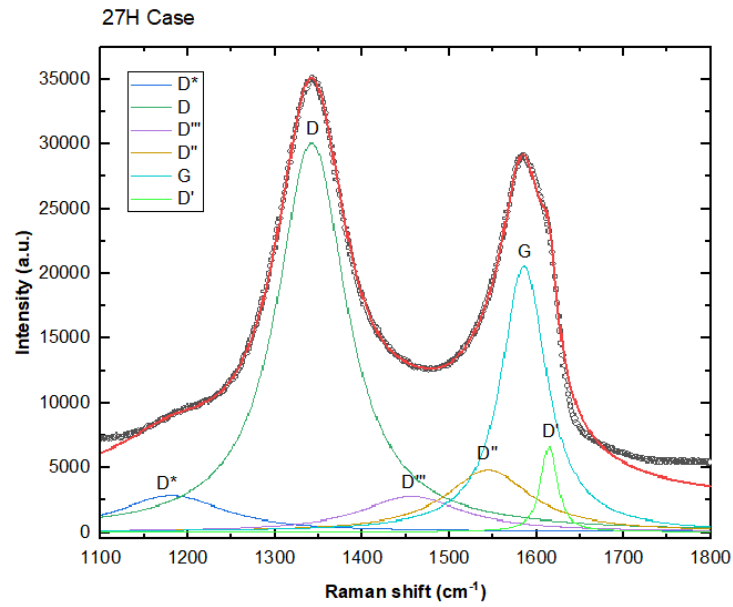
Figure 5.6: Raman bands deconvolution for 27H rGO
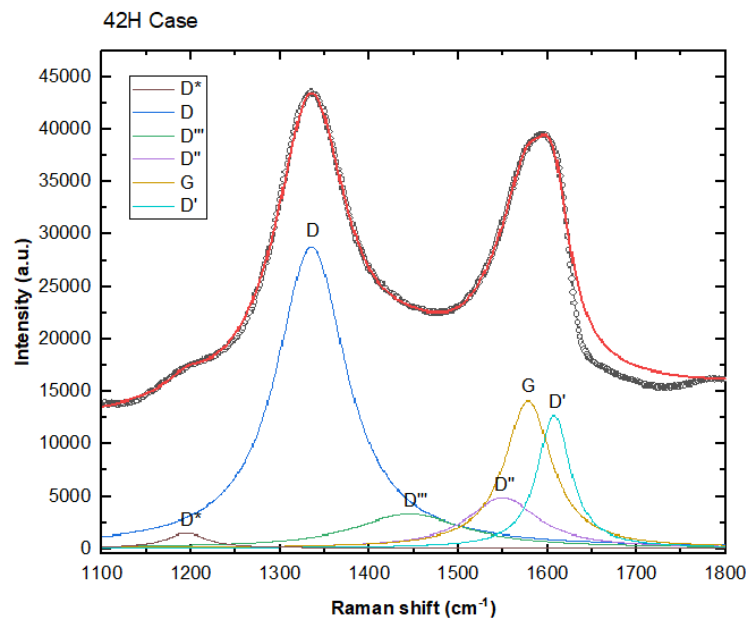
Figure 5.7: Raman bands deconvolution for 42H rGO.

Table 5.6: Raman spectra deconvolution for 27H rGO.

Peak Assignment	Raman mode	FWHM	Intensity	Fitting position [cm^{-1}]	Reference position [cm^{-1}]
C-C (graphene)	G	62.66	20497.59	1585	Claramunt[48], Vecera[49]
C$_A$-C$_B$	D	95.15	29786.568	1342	Claramunt[48], Vecera[49]
	D*	146.72	2811.36	1181	Vecera[49]
C$_B$-C$_C$	D'''	137.34	2670.22	1456	Claramunt[48], Vecera[49]
	D''	117.46	4706.41	1544	Vecera[49]
C$_C$-C$_D$	D'	23.53	6563.14	1613.5	Claramunt[48], Vecera[49]

Table 5.7: Raman spectra deconvolution for 42H rGO

Peak Assignment	Raman mode	FWHM	Intensity	Fitting position [cm^{-1}]	Reference position [cm^{-1}]
C-C (graphene)	G	64.02	14013.40	1577.5	Claramunt[48], Vecera[49]
C$_A$-C$_B$	D	94.54	28462.93	1335	Claramunt[48], Vecera[49]
	D*	56.17	1464.13	1195	Vecera[49]
C$_B$-C$_C$	D'''	146.06	3153.01	1444.5	Claramunt[48], Vecera[49]
	D''	95.77	4799.62	1549	Vecera[49]
C$_C$-C$_D$	D'	45.05	12695.97	1606.5	Claramunt[48], Vecera[49]

Bibliography

[1] Siangproh, W., Dungchai, W., Rattanarat, P., Chailapakul, O. (2011). Nanoparticle-based electrochemical detection in conventional and miniaturized systems and their bioanalytical applications: A review. Analytica Chimica Acta, 690(1), 10–25. doi:10.1016/j.aca.2011.01.054.

[2] Zhang, W., Wang, R., Luo, F., Wang, P., Lin, Z. (2019). Miniaturized electrochemical sensors and their point-of-care applications. Chinese Chemical Letters. doi:10.1016/j.cclet.2019.09.022.

[3] Yang, A. H. J., Hsieh, K., Patterson, A. S., Ferguson, B. S., Eisenstein, M., Plaxco, K. W., Soh, H. T. (2014). Accurate Zygote-Specific Discrimination of Single-Nucleotide Polymorphisms Using Microfluidic Electrochemical DNA Melting Curves. Angewandte Chemie International Edition, 53(12), 3163–3167. doi:10.1002/anie.201310059.

[4] Wang, X., Zhi, L., Tsao, N., Tomović, Ž., Li, J., Müllen, K. (2008). Transparent Carbon Films as Electrodes in Organic Solar Cells. Angewandte Chemie International Edition, 47(16), 2990–2992. doi:10.1002/anie.200704909.

[5] Bae, S., Kim, H., Lee, Y., Xu, X., Park, J.-S., Zheng, Y., . . . Iijima, S. (2010). Roll-to-roll production of 30-inch graphene films for transparent electrodes. Nature Nanotechnology, 5(8), 574–578. doi:10.1038/nnano.2010.132.

[6] Sanchez, V. C., Jachak, A., Hurt, R. H., Kane, A. B. (2011). Biological Interactions of Graphene-Family Nanomaterials: An Interdisciplinary Review. Chemical Research in Toxicology, 25(1), 15–34. doi:10.1021/tx200339h.

[7] Chaiyo, S., Mehmeti, E., Žagar, K., Siangproh, W., Chailapakul, O., Kalcher, K. (2016). Electrochemical sensors for the simultaneous determination of zinc, cadmium and lead using a Nafion/ionic liquid/graphene composite modified screen-printed carbon electrode. Analytica Chimica Acta, 918, 26–34. doi:10.1016/j.aca.2016.03.026.

[8] Lee, X. J., Hiew, B. Y. Z., Lai, K. C., Lee, L. Y., Gan, S., Thangalazhy-Gopakumar, S., Rigby, S. (2018). Review on graphene and its derivatives: Synthesis methods and potential industrial implementation. Journal of the Taiwan Institute of Chemical Engineers. doi:10.1016/j.jtice.2018.10.028.

[9] Castro Neto, A. H., Guinea, F., Peres, N. M. R., Novoselov, K. S., Geim, A. K. (2009). The electronic properties of graphene. Reviews of Modern Physics, 81(1), 109–162. doi:10.1103/revmodphys.81.109.

[10] Malik, R., Tomer, V. K., Chaudhary, V. (2019). Hybridized Graphene for Chemical Sensing. Functionalized Graphene Nanocomposites and Their Derivatives, 323–338. doi:10.1016/b978-0-12-814548-7.00016-7.

[11] Ambrosi, A., Chua, C. K., Bonanni, A., Pumera, M. (2014). Electrochemistry of Graphene and Related Materials. Chemical Reviews, **114(14)**, 7150-7188. doi:10.1021/cr500023c.

[12] Guex, L. G., Sacchi, B., Peuvot, K. F., Andersson, R. L., Pourrahimi, A. M., Ström, V., Olsson, R. T. (2017). Experimental review: chemical reduction of graphene oxide (GO) to reduced graphene oxide (rGO) by aqueous chemistry. Nanoscale, 9(27), 9562–9571. doi:10.1039/c7nr02943h.

[13] Xu, H., Dai, H., Chen, G. (2010). Direct electrochemistry and electrocatalysis of hemoglobin protein entrapped in graphene and chitosan composite film. Talanta, 81(1-2), 334–338. doi:10.1016/j.talanta.2009.12.006.

[14] Dickinson, J., Bromley, M., Andrieux, F., Boxall, C. (2013). Fabrication and Characterisation of the Graphene Ring Micro Electrode (GRiME) with an Integrated, Concentric Ag/AgCl Reference Electrode. Sensors, 13(3), 3635–3651. doi:10.3390/s130303635.

[15] Ramsden, Jeremy J. (2016). Nanotechnology, An Introduction. Second Edition. William Andrew Publishers.

[16] Toumey, C. (2009). Plenty of room, plenty of history. Nature Nanotechnology, **4(12)**, 783-784. doi:10.1038/nnano.2009.357.

[17] Goddard, W. A., Donald, W. B., Sergey, E. L., Gerald, J. I. (2003). Handbook of nanoscience, engineering, and technology. Illustrated. CRC Press. 20-28.

[18] Dubois, S. M.-M., Zanolli, Z., Declerck, X., Charlier, J.-C. (2009). Electronic properties and quantum transport in Graphene-based nanostructures. The European Physical Journal B, **72(1)**, 1–24. doi:10.1140/epjb/e2009-00327-8.

[19] Bhuyan, M. S. A., Uddin, M. N., Islam, M. M., Bipasha, F. A., Hossain, S. S. (2016). Synthesis of graphene. International Nano Letters, **6(2)**, 65-83. doi:10.1007/s40089-015-0176-1.

[20] Hernandez, Y., Nicolosi, V., Lotya, M., Blighe, F.M., Sun, Z., De, S., McGovern, I.T., Holland, B., Byrne, M., Gun'Ko, Y.K., Boland, J.J., Niraj, P., Duesberg, G., Krishnamurthy, S., Goodhue, R., Hutchison, J., Scardaci, V., Ferrari, A.C., Coleman, J.N. (2008). High-yield production of graphene by liquid-phase exfoliation of graphite. Nature Nanotechnology, 3(9), 563–568. doi:10.1038/nnano.2008.215.

[21] Weiss, N. O., Zhou, H., Liao, L., Liu, Y., Jiang, S., Huang, Y., Duan, X. (2012). Graphene: An Emerging Electronic Material. Advanced Materials, 24(43), 5782–5825. doi:10.1002/adma.201201482.

[22] Ngidi, N. P. D., Ollengo, M. A., Nyamori, V. O. (2020). Tuning the properties of boron-doped reduced graphene oxide by altering the boron content. New Journal of Chemistry. doi:10.1039/d0nj03909h.

[23] Russo, P. A., Donato, N., Leonardi, S. G., Baek, S., Conte, D. E., Neri, G., Pinna, N. (2012). Room-Temperature Hydrogen Sensing with Heteronanostructures Based on Reduced Graphene Oxide and Tin Oxide. Angewandte Chemie International Edition, 51(44), 11053–11057. doi:10.1002/anie.201204373.

[24] Wang, H. H. (2010). Flexible Chemical Sensors. Semiconductor Nanomaterials for Flexible Technologies, 247–273. doi:10.1016/b978-1-4377-7823-6.00009-x.

[25] Xu, Y., Cao, H., Xue, Y., Li, B., Cai, W. (2018). Liquid-Phase Exfoliation of Graphene: An Overview on Exfoliation Media, Techniques, and Challenges. Nanomaterials, 8(11), 942. doi:10.3390/nano8110942

[26] Yang, G., Li, L., Lee, W. B., Ng, M. C. (2018). Structure of graphene and its disorders: a review. Science and Technology of Advanced Materials, 19(1), 613–648. doi:10.1080/14686996.2018.1494493.

[27] Sfyris, D., Sfyris, G. I., Galiotis, C. (2015). Constitutive modeling of some 2D crystals: Graphene, hexagonal BN, MoS 2 , WSe 2 and NbSe 2. International Journal of Solids and Structures, 66, 98–110. doi:10.1016/j.ijsolstr.2015.03.030.

[28] Sundaram, R. S. (2014). Chemically derived graphene. Graphene, 50–80. doi:10.1533/9780857099334.1.50.

[29] Bradl H, editor. (2002). Heavy Metals in the Environment: Origin, Interaction and Remediation Volume 6. London: Academic Press.

[30] Shao, Y., Wang, J., Wu, H., Liu, J., Aksay, I. A., Lin, Y. (2010). Graphene Based Electrochemical Sensors and Biosensors: A Review. Electroanalysis, 22(10), 1027–1036. doi:10.1002/elan.200900571.

[31] Marsden, A. J., Brommer, P., Mudd, J. J., Dyson, M. A., Cook, R., Asensio, M., . . . Wilson, N. R. (2015). Effect of oxygen and nitrogen functionalization on the physical and electronic structure of graphene. Nano Research, 8(8), 2620–2635. doi:10.1007/s12274-015-0768-0.

[32] Elgrishi, N., Rountree, K. J., McCarthy, B. D., Rountree, E. S., Eisenhart, T. T., Dempsey, J. L. (2017). A Practical Beginner's Guide to Cyclic Voltammetry. Journal of Chemical Education, 95(2), 197–206. doi:10.1021/acs.jchemed.7b00361.

[33] Fu, C., Liu, C., Li, Y., Guo, Y., Luo, F., Wang, P., Lin, Z. (2016). Homogeneous Electrochemical Biosensor for Melamine Based on DNA Triplex Structure and Exonuclease III-Assisted Recycling Amplification. Analytical Chemistry, 88(20), 10176–10182. doi:10.1021/acs.analchem.6b02753.

[34] Stoller, M. D., Park, S., Zhu, Y., An, J., Ruoff, R. S. (2008). Graphene-Based Ultracapacitors. Nano Letters, 8(10), 3498–3502. doi:10.1021/nl802558y.

[35] Chekin, F., Bagheri, S., Hamid, S. B. A. (2014). Synthesis of graphene oxide nanosheet: A novel glucose sensor based on nickel-graphene oxide composite film. Russian Journal of Electrochemistry, 50(11), 1044–1049. doi:10.1134/s1023193514110020.

[36] De Silva, K. K. H., Huang, H.-H., Joshi, R. K., Yoshimura, M. (2017). Chemical reduction of graphene oxide using green reductants. Carbon, 119, 190–199. doi:10.1016/j.carbon.2017.04.025.

[37] Tang, B., Guoxin, H., Gao, H. (2010). Raman Spectroscopic Characterization of Graphene. Applied Spectroscopy Reviews, 45(5), 369–407. doi:10.1080/05704928.2010.483886.

[38] Beams, R., Gustavo Cançado, L., Novotny, L. (2015). Raman characterization of defects and dopants in graphene. Journal of Physics: Condensed Matter, 27(8), 083002. doi:10.1088/0953-8984/27/8/083002.

[39] Jorio, A., Ferreira, E. H. M., Moutinho, M. V. O., Stavale, F., Achete, C. A., Capaz, R. B. (2010). Measuring disorder in graphene with the G and D bands. Physica Status Solidi (b), 247(11-12), 2980–2982. doi:10.1002/pssb.201000247.

[40] Jorio, A., Saito, R., Dresselhaus, G., Dresselhaus, M. S. (2011). Eds. Raman Spectroscopy in Graphene related materials, 1st ed.; WILEY-VCH: Av. Antonio Carlos, 6627, CP 702, Belo Horizonte.

[41] Gomez-Navarro, C., Meyer, J. C., Sundaram, R. S., Chuvilin, A., Kurasch, S., Burghard, M., Kern, K. Kaiser, U. (2010). Atomic Structure of Reduced Graphene Oxide. Nano Letters, **10**, 1144-1148, doi:10.1021/nl9031617.

[42] Zuber, A. A., Klantsataya, E., Bachhuka, A. (2018). Biosensing . Reference Module in Materials Science and Materials Engineering. doi:10.1016/b978-0-12-803581-8.10410-2.

[43] Botas, C., Álvarez, P., Blanco, P., Granda, M., Blanco, C., Santamaría, R., Menéndez, R. (2013). Graphene materials with different structures prepared from the same graphite by the Hummers and Brodie methods. Carbon, 65, 156–164. doi:10.1016/j.carbon.2013.08.009.

[44] Perumbilavil, S., Sankar, P., Priya Rose, T., Philip, R. (2015). White light Z-scan measurements of ultrafast optical nonlinearity in reduced graphene oxide nanosheets in the 400–700nm region. Applied Physics Letters, 107(5), 051104. doi:10.1063/1.4928124.

[45] Inkson, B. J. (2016). Scanning electron microscopy (SEM) and transmission electron microscopy (TEM) for materials characterization. Materials Characterization Using Nondestructive Evaluation (NDE) Methods, 17–43. doi:10.1016/b978-0-08-100040-3.00002-x.

[46] S.J. Rowley-Neale, et al., An overview of recent applications of reduced graphene oxide as a basis of electroanalytical sensing platforms, (2017) Appl. Materials Today, doi:10.1016/j.apmt.2017.11.010

[47] A.T. Smith et al. (2019). Synthesis, properties, and applications of graphene oxide/reduced graphene oxide and their nanocomposites, Nano Materials Science, doi:10.1016/j.nanoms.2019.02.004.

[48] Claramunt, S., Varea, A., López-Díaz, D., Velázquez, M. M., Cornet, A., Cirera, A. (2015). The Importance of Interbands on the Interpretation of the Raman Spectrum of Graphene Oxide. The Journal of Physical Chemistry C, 119(18), 10123–10129. doi:10.1021/acs.jpcc.5b01590.

[49] Vecera, P., Chacón-Torres, J. C., Pichler, T., Reich, S., Soni, H. R., Görling, A., . . . Hirsch, A. (2017). Precise determination of graphene functionalization by in situ Raman spectroscopy. Nature Communications, 8, 15192. doi:10.1038/ncomms15192.

[50] Yan, J.-A., Chou, M. Y. (2010). Oxidation functional groups on graphene: Structural and electronic properties. Physical Review B, 82(12). doi:10.1103/physrevb.82.125403.

[51] Wang, J., Ma, F., Liang, W., Sun, M. (2017). Electrical properties and applications of graphene, hexagonal boron nitride (h-BN), and graphene/h-BN heterostructures. Materials Today Physics, 2, 6–34. doi:10.1016/j.mtphys.2017.07.001.

[52] Bumbrah, G. S., Sharma, R. M. (2016). Raman spectroscopy - Basic principle, instrumentation and selected applications for the characterization of drugs of abuse. Egyptian Journal of Forensic Sciences, 6(3), 209–215. doi:10.1016/j.ejfs.2015.06.001.

[53] Three-Electrode Setups | Pine Research https://pineresearch.com/shop/kb/applications/rde-and-rrde/three-electrode-setups/.

[54] Leggett A. J. (2010). Lecture 5: Graphene : Electronic band structure and Dirac fermions. web.physics.ucsb.ude./~phys123B/w2015/leggett-lecture.pdf.

[55] Pei, S., Cheng, H.-M. (2012). The reduction of graphene oxide. Carbon, 50(9), 3210–3228. doi:10.1016/j.carbon.2011.11.010.

[56] Wring, S. A., Hart, J. P. (1992). Chemically modified, carbon-based electrodes and their application as electrochemical sensors for the analysis of biologically important compounds. A review. The Analyst, 117(8), 1215. doi:10.1039/an9921701215.

[57] Elgrishi, N., Rountree, K. J., McCarthy, B. D., Rountree, E. S., Eisenhart, T. T., Dempsey, J. L. (2017). A Practical Beginner's Guide to Cyclic Voltammetry. Journal of Chemical Education, 95(2), 197–206. doi:10.1021/acs.jchemed.7b00361.

[58] Plutnar, J., Pumera, M., Sofer, Z. (2018). The chemistry of CVD graphene. Journal of Materials Chemistry C, 6(23), 6082–6101. doi:10.1039/c8tc00463c.

[59] Brownson, D. A. C., Banks, C. E. (2012). The electrochemistry of CVD graphene: progress and prospects. Physical Chemistry Chemical Physics, 14(23), 8264. doi:10.1039/c2cp40225d.

[60] Norimatsu, W., Kusunoki, M. (2014). Epitaxial graphene on SiC0001: advances and perspectives. Physical Chemistry Chemical Physics, 16(8), 3501. doi:10.1039/c3cp54523g.

[61] Rice, K. M., Walker, E. M., Jr, Wu, M., Gillette, C., Blough, E. R. (2014). Environmental mercury and its toxic effects. Journal of preventive medicine and public health = Yebang Uihakhoe chi, **47(2)**, 74-83. doi:10.3961/jpmph.2014.47.2.74.

[62] Hummers, W. S., Offeman, R. E. (1958). Preparation of Graphitic Oxide. Journal of the American Chemical Society, 80(6), 1339–1339. doi:10.1021/ja01539a017.

[63] Poh, H. L., Šaněk, F., Ambrosi, A., Zhao, G., Sofer, Z., Pumera, M. (2012). Graphenes prepared by Staudenmaier, Hofmann and Hummers methods with consequent thermal

exfoliation exhibit very different electrochemical properties. Nanoscale, 4(11), 3515. doi:10.1039/c2nr30490b.

[64] Stankovich, S., Dikin, D. A., Piner, R. D., Kohlhaas, K. A., Kleinhammes, A., Jia, Y., Ruoff, R. S. (2007). Synthesis of graphene-based nanosheets via chemical reduction of exfoliated graphite oxide. Carbon, 45(7), 1558–1565. doi:10.1016/j.carbon.2007.02.034.

[65] An Wong, C. H., Pumera, M. (2014). Highly conductive graphene nanoribbons from the reduction of graphene oxide nanoribbons with lithium aluminium hydride. J. Mater. Chem. C, 2(5), 856–863. doi:10.1039/c3tc31688b.

[66] Pei, S., Zhao, J., Du, J., Ren, W., Cheng, H.-M. (2010). Direct reduction of graphene oxide films into highly conductive and flexible graphene films by hydrohalic acids. Carbon, 48(15), 4466–4474. doi:10.1016/j.carbon.2010.08.006.

[67] Chen, W., Yan, L., Bangal, P. R. (2010). Chemical Reduction of Graphene Oxide to Graphene by Sulfur-Containing Compounds. The Journal of Physical Chemistry C, 114(47), 19885–19890. doi:10.1021/jp107131v.

[68] Li, X., Wang, H., Robinson, J. T., Sanchez, H., Diankov, G., Dai, H. (2009). Simultaneous Nitrogen Doping and Reduction of Graphene Oxide. Journal of the American Chemical Society, 131(43), 15939–15944. doi:10.1021/ja907098f.

[69] Dey, R. S., Hajra, S., Sahu, R. K., Raj, C. R., Panigrahi, M. K. (2012). A rapid room temperature chemical route for the synthesis of graphene: metal-mediated reduction of graphene oxide. Chemical Communications, 48(12), 1787. doi:10.1039/c2cc16031e.

[70] Basirun, W. J., Sookhakian, M., Baradaran, S., Mahmoudian, M. R., Ebadi, M. (2013). Solid-phase electrochemical reduction of graphene oxide films in alkaline solution. Nanoscale Research Letters, 8(1), 397. doi:10.1186/1556-276x-8-397.

[71] Kim, Y.-K., Kim, M.-H., Min, D.-H. (2011). Biocompatible reduced graphene oxide prepared by using dextran as a multifunctional reducing agent. Chemical Communications, 47(11), 3195. doi:10.1039/c0cc05005a.

[72] Kuila, T., Bose, S., Khanra, P., Mishra, A. K., Kim, N. H., Lee, J. H. (2012). A green approach for the reduction of graphene oxide by wild carrot root. Carbon, 50(3), 914–921. doi:10.1016/j.carbon.2011.09.053.

[73] Akhavan, O., Ghaderi, E. (2012). Escherichia coli bacteria reduce graphene oxide to bactericidal graphene in a self-limiting manner. Carbon, 50(5), 1853–1860. doi:10.1016/j.carbon.2011.12.035.

[74] Liu, J., Fu, S., Yuan, B., Li, Y., Deng, Z. (2010). Toward a Universal "Adhesive Nanosheet" for the Assembly of Multiple Nanoparticles Based on a Protein-Induced Reduction/Decoration of Graphene Oxide. Journal of the American Chemical Society, 132(21), 7279–7281. doi:10.1021/ja100938r.

[75] Chen, D., Li, L., Guo, L. (2011). An environment-friendly preparation of reduced graphene oxide nanosheets via amino acid. Nanotechnology, 22(32), 325601. doi:10.1088/0957-4484/22/32/325601.

[76] Pacyna, J. M., Travnikov, O., De Simone, F., Hedgecock, I. M., Sundseth, K., Pacyna, E. G., Kindbom, K. (2016). Current and future levels of mercury atmospheric pollution on a global scale. Atmospheric Chemistry and Physics, **16(19)**, 12495-12511. doi:10.5194/acp-16-12495-2016.

[77] Cui, L., Wu, J., Ju, H. (2015). Electrochemical sensing of heavy metal ions with inorganic, organic and bio-materials. Biosensors and Bioelectronics, **63**, 276-286. doi:10.1016/j.bios.2014.07.052.

[78] D. Oh, K. Mun, H. Lee, J. Yoo, "Frequency-Temperature Characteristics of AT-Cut Crystal Resonator and Oscillator Utilizing Relaxator Ceramic as Load Capacitor"', *Jpn. J. Appl. Phys.*, **44**, 9A, (2005).